Applied Computing and Geosciences 31 (2026) 100377

Contents lists available at ScienceDirect

Applied Computing and Geosciences

journal homepage: www.sciencedirect.com/journal/applied-computing-and-geosciences

Towards surface-based hydraulic conductivity mapping using seismoelectric signals and data-driven models

Roberto Aedo-García [a,*], Jorge Jímenez [b], Felipe Quiero [e], Miguel Valdebenito [a,b], Yamisleydi Salgueiro [c], Carlos Rey [d], Gonzalo S. Saldías [a,f]

[a] Departamento de Física, Facultad de Ciencias, Universidad del Bío-Bío, Concepción, 4081112, Biobío, Chile
[b] G-Strata, Cosme Churruca 400, Concepción, Biobío, Chile
[c] Department of Industrial Engineering, Faculty of Engineering, Universidad de Talca, Campus Curicó, 3341717, Maule, Chile
[d] Departamento de Ingeniería Industrial, Universidad del Bío-Bío, Concepción, 4030000, Biobío, Chile
[e] Departamento de Física, Universidad Andres Bello, Santiago, Chile
[f] Centro de Investigación Oceanográfica COPAS Coastal, Universidad de Concepción, Concepción, Chile

ARTICLE INFO

Dataset link: https://doi.org/10.5281/zenodo.17234793

Keywords:
Seismoelectric method
Vertical hydraulic conductivity
Hydrogeophysics
Machine learning
Feature engineering
Subsurface mapping

ABSTRACT

Estimating vertical hydraulic conductivity (K_v) in semi-arid basins is challenging because lithological heterogeneity limits the representativeness of sparse hydraulic measurements. This study evaluates a surface-based seismoelectric workflow for inferring depth-resolved K_v profiles without using drilling information during model development. Borehole data were reserved for external validation. The workflow integrates field acquisition, geospatial data synthesis, signal conditioning, physically guided feature engineering, supervised regression benchmarking, and hydrogeological expert appraisal. Its main contribution is a drilling-independent modeling strategy that translates surface seismoelectric attributes into vertical K_v profiles. This provides pre-drilling information for well siting, screen-interval design, and planning of drilling and completion costs. A high-density survey was conducted in the Ñuble Region of central Chile using a dual-channel seismoelectric system with investigation depths of up to 200 m. More than 500 georeferenced stations were acquired. Seismoelectric attributes derived from the dual-channel response, together with topographic descriptors, were used to train and compare multiple regression models. Compared with a baseline configuration based only on raw voltage and depth, the augmented model showed stronger cross-validated performance. The coefficient of determination increased from $R^2 = 0.711$ to $R^2 = 0.968$, RMSE decreased from 3.534 to 1.305 m/d, and MAE decreased from 1.368 to 0.546 m/d. The predicted K_v profiles better preserved persistent high- and low-conductivity intervals and abrupt vertical transitions than the baseline model. They were also consistent with independent lithostratigraphic evidence and post-drilling yield verification at the validation site. Profile-level smoothing with Savitzky–Golay and wavelet filters improved visual continuity while preserving the dominant conductivity contrasts. These results support the use of surface seismoelectric data combined with supervised learning to reconstruct vertical K_v structure in geologically complex and data-scarce settings.

1. Introduction

Characterizing saturated hydraulic conductivity (K), particularly its vertical component (K_v), is fundamental for groundwater management, contaminant transport assessment, and predictive flow modeling (Sun et al., 2024; Osta et al., 2023; Jiang et al., 2022). Recent studies illustrate this relevance from complementary perspectives. Sun et al. (2024) compared several approaches for estimating K in heterogeneous aquifers and showed that conventional, direct-push, and inverse-modeling methods can yield different levels of predictive reliability for groundwater-flow simulations. Osta et al. (2023) showed that hydraulic parameters, including hydraulic conductivity, transmissivity, drawdown, well efficiency, and safe yield, are central to aquifer sustainability assessment and groundwater-management planning in arid reclamation settings. These contributions reinforce that hydraulic conductivity is not only a model parameter, but also a decision-relevant variable for groundwater development, well performance, and aquifer sustainability. Vertical conductivity controls hydraulic exchange between layers and therefore strongly influences groundwater storage and flow dynamics. However, estimating K_v remains difficult because it

* Corresponding author.
E-mail address: raedogar@ubiobio.cl (R. Aedo-García).

https://doi.org/10.1016/j.acags.2026.100377
Received 20 January 2026; Received in revised form 1 June 2026; Accepted 23 June 2026
Available online 8 July 2026

depends on lithological heterogeneity, anisotropy, pore connectivity, fracture networks, and scale effects, often leading to substantial discrepancies between laboratory and in situ measurements (Medici and West, 2021; Shepley, 2024; Nam et al., 2021).

Hydraulic behavior in porous and fractured media is controlled by lithology, pore structure, mineralogical composition, thermal evolution, organic content, and tectonic history. Recent studies in unconventional reservoirs have shown that pore connectivity and fracture development can modify permeability and preferential flow pathways (Wang et al., 2026; Zhang et al., 2022, 2017, 2026). Although these studies focus on shale and tight reservoirs rather than unconsolidated alluvial systems, they support a broader hydrogeological principle: surface-based characterization methods should capture vertical hydraulic contrasts and subsurface architecture, not only broad lithological classes. Fracture systems may act as both storage domains and preferential flow conduits, while their saturation state often requires indirect assessment (Zhang et al., 2025).

Because direct hydraulic information is typically sparse, hydrogeophysical methods are widely used to extend subsurface characterization beyond wells and local tests (e.g., Binley et al., 2010, 2015; Dumont and Singha, 2024). Electrical resistivity tomography (ERT) and induced polarization (IP) are commonly applied to delineate lithological contrasts and infer hydraulic properties after calibration with borehole information (Wang et al., 2025; Jarzyna et al., 2019; Oldenborger and Paradis, 2023). Nevertheless, the relationship between electrical response and hydraulic conductivity is indirect and often non-unique, because electrical signals are affected by grain size, saturation, clay content, pore-fluid chemistry, and cementation (Koch et al., 2011; Zheng et al., 2021). Inversion regularization may also reduce sensitivity to thin low-permeability intervals or sharp hydraulic boundaries that are critical for vertical flow (Friedel, 2003).

Seismoelectric methods provide a complementary perspective because they arise from electrokinetic coupling between seismic wave propagation and fluid flow in saturated porous media (Zhu et al., 2008; Martins-Gomes et al., 2023). In the framework developed by Pride (1994), seismic perturbations induce relative motion between pore fluid and solid matrix, generating electrical and electromagnetic responses linked to permeability, porosity, and saturation (Cosenza et al., 2009; Grobbe et al., 2020; Abbas et al., 2022). This physical connection makes seismoelectric measurements attractive in settings where conventional geophysical proxies remain hydraulically ambiguous (Lochbuhler et al., 2013; Xie et al., 2021; Chicco et al., 2023).

Despite this potential, transforming seismoelectric observations into quantitative estimates of K_v remains challenging. The signals are influenced by coupled mechanical, hydraulic, and electrical processes; field measurements commonly contain substantial noise; and direct hydraulic tests such as pumping or slug tests remain spatially limited and expensive (Sánchez-Vila and Tartakovsky, 2007; Shepley, 2024; Fan et al., 2025). A methodological gap therefore remains between approaches that provide indirect hydraulic information over large areas and approaches that provide direct but spatially sparse measurements.

Machine learning (ML) offers a practical way to address this gap. Instead of relying on explicit site-specific inversion schemes, supervised ML models can learn nonlinear relationships between observed geophysical attributes and hydraulic targets directly from data (ur Rehman et al., 2022; Nguyen and Vu, 2024). Related approaches have been applied to groundwater-level forecasting, permeability prediction, pore-pressure estimation, and reservoir characterization (Feng et al., 2024; Radwan et al., 2022; Zanganeh Kamali et al., 2022; Albalasmeh et al., 2022; Oldenborger and Paradis, 2023; Huang et al., 2025). These studies indicate that data-driven models are most useful when linked to physically meaningful predictors, independent validation data, or geophysical attributes that encode subsurface heterogeneity. This is particularly relevant for K_v estimation, where direct measurements are sparse and vertical hydraulic contrasts may not be captured by raw geophysical amplitudes alone. ML does not replace physical interpretation, but it provides a useful framework when hydraulic data are limited and subsurface heterogeneity is strong.

The present study builds on this premise by combining surface-based seismoelectric measurements with supervised regression to estimate vertical hydraulic conductivity (K_v). Borehole information is used only for external validation rather than for model development. The workflow integrates field acquisition, geospatial synthesis, signal conditioning, physically informed feature engineering, automated benchmarking of regression models, and hydrogeological expert appraisal. The objective is to evaluate whether surface-based seismoelectric attributes, combined with supervised regression and topographic context, can provide spatially coherent estimates of K_v that are consistent with independent hydrostratigraphic evidence.

2. Materials and methods

This study presents an end-to-end framework that combines surface seismoelectric measurements with supervised regression to estimate vertical hydraulic conductivity (K_v) in a semi-arid agricultural basin in central Chile. The workflow comprises five stages: (1) definition of the seismoelectric framework and regression target; (2) field data acquisition and site characterization; (3) geospatial integration and training-sample consolidation; (4) signal conditioning and multidimensional feature engineering; and (5) model training, cross-validation, and expert-based spatial assessment of the predicted profiles.

2.1. Theoretical framework: Electrokinetic coupling and hydraulic scaling

When a seismic wave propagates through a saturated porous medium, transient pore-pressure gradients drive pore-fluid motion relative to the mineral frame. Mineral surfaces in contact with groundwater develop an electrical double layer (Revil and Pezard, 1999; Revil and Jardani, 2013). The relative motion between pore fluid and solid matrix advects mobile ions in the diffuse layer, generating a streaming current and a measurable surface electrical potential (Pride, 1994; Revil et al., 2003). The physical sequence can therefore be summarized as follows: seismic perturbation → pore-pressure gradient → streaming current → electrical response (Fig. 2b).

At the continuum scale, total current density combines ordinary electrical conduction with an electrokinetically induced streaming term,

$$\mathbf{J} = -\sigma \nabla V + \mathbf{J}_s, \qquad \mathbf{J}_s = -L \nabla p, \tag{1}$$

where σ is bulk electrical conductivity, V is electric potential, p is pore pressure, and L is the electrokinetic coupling coefficient (Pride, 1994). Applying charge conservation ($\nabla \cdot \mathbf{J} = 0$) gives

$$\nabla \cdot (\sigma \nabla V) = -\nabla \cdot (L \nabla p), \tag{2}$$

which indicates that pressure transients behave as distributed electrical sources, while σ controls how the induced potential propagates through the medium (Revil et al., 2003; Jardani et al., 2007).

Under approximately uniform pore-water chemistry, the streaming-potential coupling coefficient can be expressed as

$$C_{sp} \equiv \frac{\Delta V}{\Delta p} \approx -\frac{L}{\sigma} \approx \frac{\varepsilon \zeta}{\eta \sigma_f}, \tag{3}$$

where ε is dielectric permittivity, ζ is zeta potential, η is dynamic viscosity, and σ_f is pore-fluid conductivity (Revil et al., 2001; Binley et al., 2015). If these properties vary modestly across the survey area, spatial changes in the seismoelectric response can be interpreted primarily in terms of pressure diffusion and hydraulic connectivity, rather than fluid-chemistry variability alone.

The link with hydraulic conductivity enters through the transient hydraulic head perturbation h', governed by

$$S_s \frac{\partial h'}{\partial t} = \nabla \cdot (K \nabla h'), \tag{4}$$

where S_s is specific storage and K is hydraulic conductivity ($K = \rho g k/\eta$, with k denoting intrinsic permeability). For a characteristic length ℓ, the pressure-diffusion time scale is

$$t_c \sim \frac{\ell^2 S_s}{K}. \tag{5}$$

Higher-conductivity intervals diffuse pressure perturbations more rapidly, which may produce lower signal amplitudes, shorter durations, and steeper spectral decay. Lower-conductivity intervals can sustain sharper pressure gradients for longer (Martínez-Ballesta et al., 2011; Jardani et al., 2007; Revil et al., 2003). In layered systems, vertical changes in K_v can therefore leave detectable signatures in seismoelectric time- and frequency-domain attributes. This provides the physical basis for using these attributes as predictors of depth-dependent K_v in the supervised regression workflow described below (Hu et al., 2023; Thanh et al., 2020).

2.2. Study area and field acquisition

The experimental campaign was carried out in the Ñuble Region of central Chile, focusing on the alluvial deposits of the Itata and Ñuble river basins (Fig. 1). The area belongs to the Central Valley of Chile, an Andean forearc domain where tectonic subsidence and fluvial, glacial, volcanic, and volcanosedimentary processes have produced a thick and heterogeneous sedimentary fill (Aguirre et al., 2022; Servicio Nacional de Geología y Minería, 2003). Previous hydrogeophysical work in the Ñuble aquifer indicates hydrogeological potential between approximately 50 and 300–500 m depth, above a sedimentary basin that may exceed 1000 m in thickness (Aguirre et al., 2022). Near-surface and intermediate-depth units include Pleistocene–Holocene sedimentary rocks, alluvial to colluvial deposits, mass-wasting deposits, subordinate fluvioglacial and deltaic deposits, volcanic and pyroclastic units, morainic deposits towards the Andean foothills, and fluvial sandstones and siltstones towards the central and western sectors of the basin (Aguirre et al., 2022; Servicio Nacional de Geología y Minería, 2003).

This setting is suitable for testing a surface-based K_v mapping workflow because hydraulic conductivity is expected to vary strongly with depth and laterally across the basin. Hydrogeological interpretations of the Biobío–Itata system describe aquifer units dominated by fine deposits, with restricted sectors of medium to high permeability and more extensive intervals of medium to low permeability (Aguirre et al., 2022). In the Ñuble aquifer, permeability within the upper 100–200 m is influenced by fine sediment content, cementation, compaction, and volcanosedimentary layering, while information for deeper aquifers remains sparse (Aguirre et al., 2022). The region is also affected by the long-lasting central Chile megadrought and increasing water stress associated with reduced water availability and agricultural demand (Garreaud et al., 2017, 2020; Alvarez-Garreton et al., 2021; Boisier et al., 2025; Zapata Márquez, 2022). The coexistence of geological heterogeneity, limited deep hydraulic information, and high groundwater demand makes the Ñuble sector an appropriate test site for evaluating whether seismoelectric attributes can recover depth-dependent contrasts in K_v before drilling. The station layout shown in Fig. 1 includes scale bars at regional, basin, survey-sector, and validation-transect levels to support interpretation of survey extent and inter-station spacing.

Station spacing was not uniform because the layout was designed to cover the main geomorphological sectors while accommodating terrain and land-access constraints. Higher local station density was used along the validation transect to support profile-level comparison with lithostratigraphic and post-drilling evidence. Subsurface conditions were investigated using the AquaLocate GF6 seismoelectric system at more than 500 georeferenced stations distributed over approximately 18.5 km^2, corresponding to an average sampling density of $\rho_s \approx 27$ stations km^{-2}. The mean nearest-neighbor spacing was about 150 m, and inter-station distances ranged from 0.1 to 1.0 km. This design provided broad regional coverage while preserving sufficient local density to resolve lateral variability in the seismoelectric response.

At each station, two-channel voltage profiles were recorded to a target depth of 200 m to capture the transient electrical response associated with seismic wave propagation through the variably saturated subsurface. Predictive attributes were extracted using the multi-channel seismoelectric spectral ratio (MC-SESR) method. In this approach, amplitude spectra from the depth-converted transients of both voltage channels were calculated and expressed as a frequency-dependent spectral ratio. This representation enhances coherent anomalies between channels while reducing source-amplitude variations and common-mode noise. The analysis was restricted to the frequency interval where the seismoelectric response remained stable after preprocessing. The resulting ratio curves were used to identify spectral signatures associated with vertical hydraulic conductivity contrasts and the water-table transition. Relative to single-channel spectral analysis, MC-SESR emphasizes differential subsurface responses rather than absolute spectral amplitudes.

Fig. 2 summarizes the field acquisition setup, the physical interpretation adopted in this study, and the operational sequence followed during data collection. The acquisition workflow began with survey planning and station georeferencing, followed by deployment of the GF6 unit, seismic source, and two surface voltage channels at each station. Paired V1 and V2 voltage responses were then recorded to a target investigation depth of 200 m. For each station, the field record included the point identifier, geographic coordinates, depth coordinate, and two voltage-channel amplitudes. These raw station records were exported together with the KML/KMZ geolocation files and used as input for the data synthesis procedure described in Section 2.2.

2.3. Data synthesis and sample architecture

A centralized modeling database was assembled by integrating station geolocation records from KML/KMZ files with the primary seismoelectric outputs. The raw field data included the point identifier, latitude, longitude, depth, voltage amplitudes from channels A and B, and the expert-interpreted hydraulic conductivity product. For computational consistency, the measured channels V_1 and V_2 were stored as `BLUE Channel(Z)` and `RED Channel(Z)`, respectively (Fig. 3). Spatial integration linked each depth-resolved profile to its corresponding georeferenced station record, so that each observation inherited the latitude and longitude of its parent station. Because elevation was not available in the original records, it was assigned from the geographic coordinates of each point using an automated elevation-retrieval routine and stored as the topographic descriptor `Cota` (m a.s.l.). The relative elevation contrast between adjacent stations was then computed as `cotadiff`.

The resulting merged structure combines station-level spatial descriptors, depth-resolved seismoelectric measurements, engineered predictors, and the supervisory target `HydCon(Z)` in a single modeling table (Fig. 3).

The database was organized at the depth-sample level. Each observation corresponds to a discrete depth z within a station profile, so that each vertical survey is represented as a sequence of records spanning $z \in [0, 200]$ m. The complete modeling dataset comprises 437,663 depth-level observations from more than 500 georeferenced stations. The final table contains 23 columns: one station identifier (`name`), one along-profile spatial coordinate (`Distance(Y)`), one depth coordinate (`Depth(X)`), two topographic descriptors (`Cota`, `cotadiff`), two raw seismoelectric channels (`BLUE Channel(Z)`, `RED Channel(Z)`), fourteen engineered signal features, and the supervisory target `HydCon(Z)`. Although the table contains 437,663 depth-level records, the effective number of independent spatial units is substantially smaller because samples are nested within station profiles.

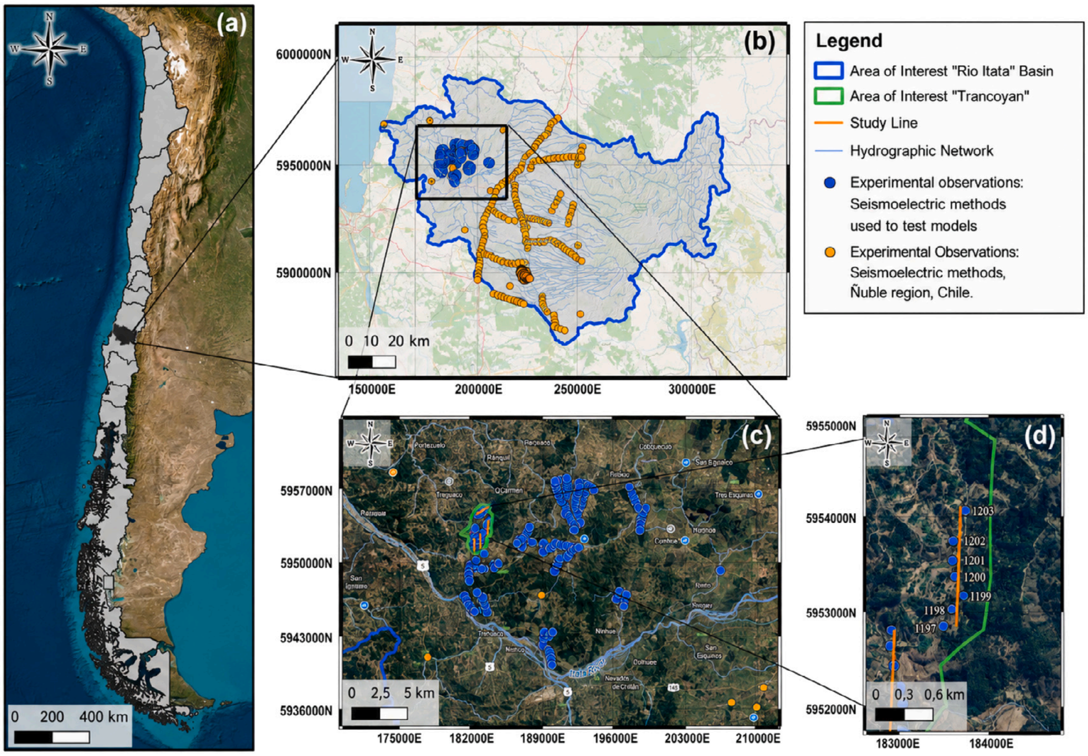

Fig. 1. Study area and spatial distribution of the seismoelectric survey stations in the Itata–Ñuble alluvial system, central Chile. (a) Regional location of the study area within Chile. (b) Location of the Río Itata basin, Trancoyan area of interest, hydrographic network, study lines, and regional seismoelectric observations. (c) Detailed view of the main survey sector, showing the spatial distribution of the georeferenced stations used to construct the modeling dataset. (d) Zoomed view of the validation transect, including stations 1197–1205, where the local station density is higher to support profile-level comparison with lithostratigraphic and post-drilling evidence. Scale bars were included in all spatial panels to facilitate interpretation of survey extent, inter-station spacing, and local density variations. The irregular station distribution reflects the combined need to cover the main geomorphological units, follow accessible survey lines, and obtain higher spatial detail in the validation area.

This representation preserves the vertical structure of each profile while allowing the model to capture lateral variability between stations.

Most variables were fully populated across the 437,663 observations. Two exceptions are relevant for reproducibility. First, the `name` column contained 254,590 non-null values because, for a subset of records, the station identifier could not be recovered during the merge with KMZ metadata. These records retained complete geophysical, positional, and topographic information and were therefore preserved for model training, but they were excluded from analyses requiring explicit station labels or profile-level traceability. Second, the `A/B` ratio was initially stored as `object` rather than `float64`, reflecting non-finite values generated by divisions involving near-zero `RED Channel(Z)` amplitudes. Before model fitting, this variable was cast to numeric format and non-finite entries were replaced by the column median.

The regression target is the depth-dependent vertical hydraulic conductivity profile inferred by expert interpretation, denoted `HydCon(Z)` (m/d). `HydCon(Z)` was generated by G-Strata before the machine-learning stage as an expert-interpreted conductivity product derived from the field seismoelectric survey. It was used only as the supervised learning target and was not included among the predictor variables. The predictor matrix was constructed separately from depth, dual-channel voltage measurements, station-level spatial descriptors, topographic variables, and engineered signal attributes. Thus, the model was trained to approximate a pre-existing `HydCon(Z)` profile from independently assembled predictors, rather than to reproduce a target generated from the same engineered feature set used during model fitting.

For station s, the corresponding target is expressed as the vector $K_v^{(s)}(z)$ over $z \in [0, 200]$ m, and the learning objective is to estimate $\hat{K}_v(z)$ from co-located predictors. Accordingly, each station contributes paired samples $\{(\mathbf{x}_{s,z}, K_v^{(s)}(z))\}_z$, where $\mathbf{x}_{s,z}$ contains depth, dual-channel measurements, spatial descriptors, topographic context, and engineered signal attributes.

For model development, the full dataset was partitioned into a training set (70%) and a held-out test set (30%), yielding approximately 306,364 training samples and 131,299 hold-out samples. This proportion was selected to retain a large unseen subset for robustness assessment while preserving sufficient training volume for cross-validated fitting of flexible regression models. Sample selection was defined at the depth-record level after data integration and quality control, retaining observations with valid predictors and target values. Because records within the same profile are not independent along z, model evaluation accounted for within-profile dependence through standard k-fold cross-validation combined with an independent spatial hold-out (Fig. 1c). This design provides a more demanding test of generalization under lateral geological variability and reduces the optimistic bias that can arise from purely random partitioning in spatially structured hydrogeophysical datasets (Oldenborger and Paradis, 2023; Tilahun and Korus, 2023).

2.4. Signal conditioning and physically guided feature engineering

Fig. 4 summarizes the workflow used to condition the seismoelectric signals before model fitting. The procedure was implemented in Python using NumPy, SciPy, and PyWavelets, and comprised three main operations. First, raw traces were converted from sample index to physical time using the 3 kHz acquisition frequency. Second, the time axis was mapped to depth ($z \in [0, 200]$ m) using a layered velocity scheme, with piecewise scale factors of ×800, ×1500, and ×3000 for shallow, intermediate, and deep intervals, respectively. Third, a 50 Hz notch

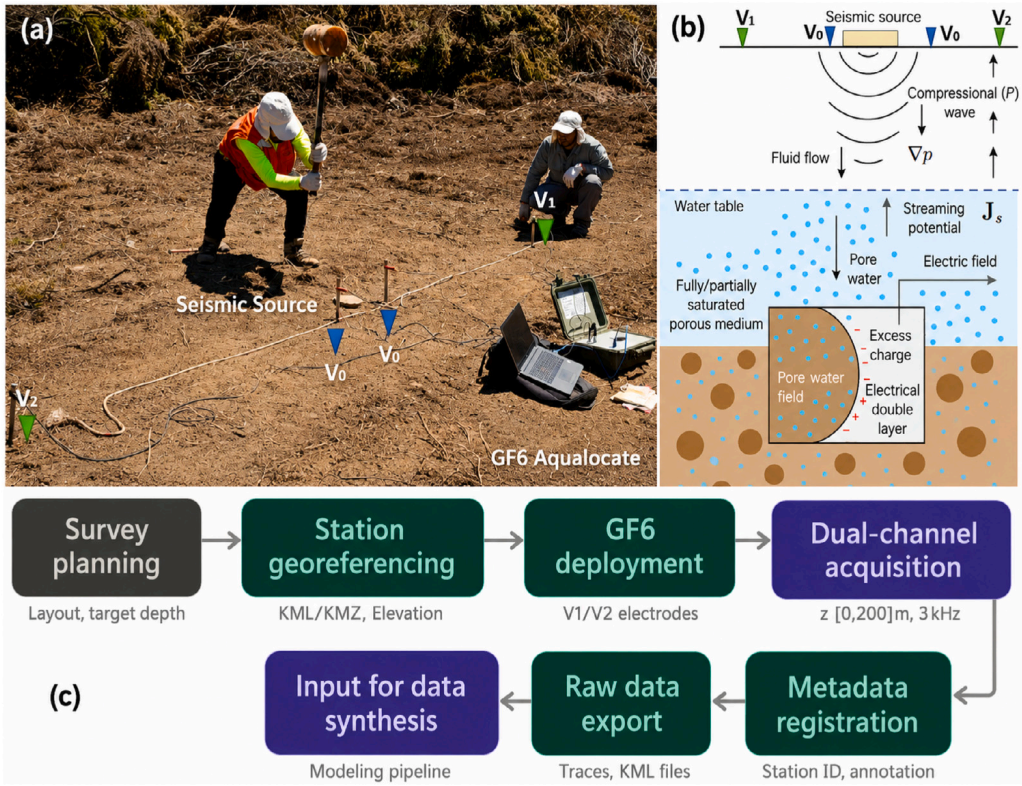

Fig. 2. Field acquisition, seismoelectric coupling mechanism, and acquisition-to-data workflow. (a) Surface deployment of the GF6 system, seismic source, and two voltage channels. (b) Schematic representation of the seismoelectric coupling mechanism linking seismic-wave-induced pressure gradients, relative fluid flow, and the measured surface electrical response across subsurface layers. (c) Operational flowchart summarizing the sequence from survey planning and station georeferencing to GF6 deployment, dual-channel voltage recording, field metadata registration, raw data export, and subsequent data synthesis.

Name	Latitude	Longitude	Elevation	Distance (Y)	Depth (Z)	Blue Channel (Z)	Red Channel (Z)	HydCon (Z)
1096	-36,5024	-72,44912	154	0	0	-0,003353	-0,003353	7,234
1096	-36,5024	-72,44912	154	0	-0,04	-0,0033	-0,0033	7,2441
1096	-36,5024	-72,44912	154	0	-0,08	-0,0033	-0,0033	6,8545

Fig. 3. Integrated project visualization: (a) geospatial information in KMZ/KML format, (b) field-acquired seismoelectric data, and (c) the integrated modeling table. The workflow links station coordinates to raw voltage profiles, assigns elevation from geographic position, and appends engineered features together with the supervisory target `HydCon(Z)`. This structure preserves the connection between station location, depth-resolved signal response, topographic context, and the target variable used for supervised regression.

filter was applied to attenuate power-line contamination under Chilean field conditions. The resulting depth-resolved dual-channel profiles were then used for feature extraction.

This transformation places the analysis in the depth domain, where the target conductivity structure is interpreted. Rather than imposing a hydrogeophysical forward model during regression, the approach allows the predictor set to capture relations observed in the depth-resolved responses while retaining a physically interpretable connection with the acquisition process (cf. Hu et al., 2023; Oldenborger and Paradis, 2023).

The conditioning stage was designed to reduce the main sources of signal degradation without erasing sharp vertical transitions that may carry lithological or hydraulic meaning. As shown in Fig. 4, the

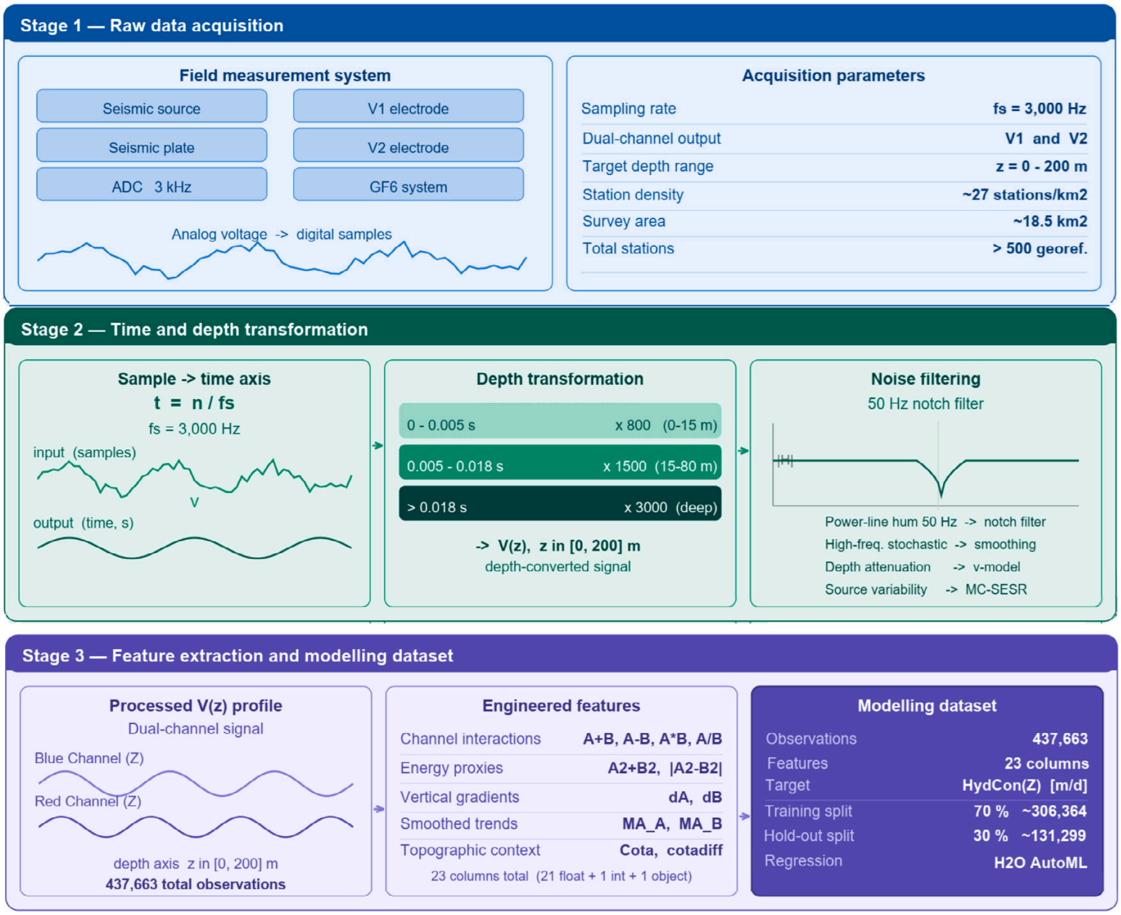

Fig. 4. Seismoelectric acquisition, conditioning, and feature-extraction workflow. The figure summarizes the sequence from field acquisition of the dual-channel seismoelectric response to signal conditioning, depth referencing, and construction of engineered predictors. The cross-channel interaction panel compares the conditioned responses of channels A and B, with axes and units explicitly labeled to clarify how the two recorded signals were jointly interpreted. This comparison motivated the inter-channel attributes used in the augmented model, including $A-B$, A/B, $A \cdot B$, A^2-B^2, and $|A-B|$, which were designed to capture channel asymmetry, proportional scaling, and nonlinear coupling in the seismoelectric response.

workflow addressed four effects: 50 Hz electrical interference, attenuated with the notch filter; high-frequency ambient and mechanical noise, reduced through local smoothing; depth-dependent amplitude loss, compensated through the layered velocity mapping; and source variability between stations, normalized through the dual-channel MC-SESR spectral ratio described in Section 2.2. The objective was to suppress spurious fluctuations while preserving hydrostratigraphically relevant discontinuities (Shepley, 2024).

Physically guided feature engineering was based on the assumption that the relation between seismoelectric attributes and K_v is nonlinear and medium dependent. This assumption is consistent with the known dependence of permeability on pore geometry and porosity (Costa, 2006), and with hydrogeophysical evidence showing that grain-size distribution, pore-space structure, and channel relationships can affect both hydraulic conductivity and geophysical response (Koch et al., 2011; Hu et al., 2023). The engineered predictors were therefore designed as interpretable proxies rather than direct measurements of K_v. They were intended to help the model recover hydraulic patterns that are not represented by raw amplitudes and depth alone.

The predictor vector $\mathbf{x}$ was expanded with attributes derived from the relation between `BLUE Channel(Z)` and `RED Channel(Z)`. To keep the feature set interpretable, the variables were grouped into five types: central tendency, represented by the mean signal $(A+B)/2$; channel contrast, including $A-B$, $|A-B|$, A^2-B^2, and $\sqrt{|A^2-B^2|}$; nonlinear interaction, including $A \cdot B$, A/B, $A+B^2$, and $A-B^2$; energy-related magnitude, represented by A^2+B^2; and first-order vertical change, expressed as $dA = A_t - A_{t-1}$ and $dB = B_t - B_{t-1}$. Short-window moving averages of A and B (window n=2) were also included to represent local depth trends. In addition, two contextual topographic descriptors, absolute elevation (`Cota`) and relative elevation contrast (`cotadiff`), were incorporated to account for hydrogeological organization linked to terrain position. The full mathematical definitions are provided in Table 9. This choice is consistent with recent hydrogeophysical studies showing that relations between channels often carry more predictive value than raw measurements considered in isolation (Hu et al., 2023; Oldenborger and Paradis, 2023).

No pre-filtering stage was used to remove predictors before training. The initial attribute set was defined a priori from electrokinetic reasoning (Section 2.1) and retained inter-channel relations and topographic descriptors considered physically interpretable. During model fitting, the effective contribution of each variable was controlled by the regularization and structural constraints of the base learners within `H2O AutoML`, including L1/L2 penalties in GLM, minimum node size in DRF, and shrinkage in XGBoost. Predictor relevance was then examined a posteriori through SHAP attribution analysis (Figs. 7 and 9), which showed that only a subset of the engineered variables dominated the final predictive behavior.

2.4.1. Profile-level post-processing filters

Several post-processing filters were applied to the predicted $K_v(z)$ profiles to examine whether limited smoothing could improve morphological continuity without obscuring hydrogeologically meaningful contrasts. These filters were applied only after model inference and were used for profile comparison and visualization, not to improve predictive skill against external data. The final parameter values used for the reported filtered profiles are summarized in Table 8 to ensure reproducibility.

Filter tuning was performed at the profile level. For each validation profile, the predicted $K_v(z)$ sequence was ordered by increasing depth and treated as a one-dimensional vertical signal. Candidate filters were applied to the complete predicted profile using the same depth sampling as the model output. The tuning criterion was qualitative–quantitative: acceptable smoothing had to reduce short-wavelength oscillations while preserving the depth position, amplitude contrast, and sharpness of the main hydrostratigraphic transitions. To avoid over-smoothing, each filtered profile was compared with the original unfiltered prediction using visual inspection of vertical morphology and scatter plots against the unfiltered profile. The R^2 values reported for these scatter plots were interpreted only as structural-similarity indicators between filtered and unfiltered predictions, not as independent validation metrics.

A Savitzky–Golay filter was tested as a local polynomial smoother. Window lengths between 20 and 40 samples and polynomial orders between 2 and 4 were evaluated, with boundary handling explored using the `mirror`, `constant`, `nearest`, `wrap`, and `interp` modes. The final configuration, window length = 35 samples, polynomial order = 4, and `mode = nearest`, provided the best compromise between local roughness reduction and preservation of local extrema and steep vertical gradients.

Wavelet denoising was examined as a multiscale alternative. The tested mother wavelets included `haar`, `db2`, `db4`, `sym4`, `sym8`, `coif1`, `bior3.5`, `rbio3.1`, and `dmey`, combined with different decomposition levels, thresholding strategies, shrinkage rules, and padding modes. Level 1 produced mild filtering with high detail retention, levels 2–3 provided intermediate smoothing, and levels ≥4 imposed stronger attenuation of rapid fluctuations, with greater risk of erasing diagnostically relevant structure. The final configuration used the `db4` wavelet at level 4, with approximation-only reconstruction after removal of detail coefficients, because it provided effective multiscale smoothing while maintaining the principal conductivity contrasts.

Frequency-domain and digital filters were also evaluated to compare alternative smoothing behaviors. The FFT low-pass filter transformed each profile into the frequency domain, retained low-frequency components according to the parameter `cutoff_ratio`, removed higher-frequency components, and reconstructed the profile by inverse transformation. A notch filter was considered where narrow-band 50 Hz electrical contamination was suspected. Butterworth filters were tested with orders from 1 to 3 and cutoff frequencies between 35 and 150, while Chebyshev filters were tested over the same order range with cutoff frequencies from 35 to 170 and controlled passband ripple. Together, these filters were used to examine the trade-off between denoising strength, preservation of vertical gradients, and retention of hydrostratigraphically relevant contrasts.

2.5. Predictive architecture and robustness protocols

The predictive modeling workflow followed a structured sequence of data partitioning, model training, internal validation, model comparison, and external performance assessment, as summarized in Fig. 5.

Regression analysis was conducted with the `H2O AutoML` framework (LeDell and Poirier, 2020), which automatically trained and benchmarked several regression families under a common workflow. The evaluated learners included generalized linear models (GLM), distributed random forests (DRF), XGBoost gradient-boosted trees, deep neural networks, and stacked ensembles built from the best-performing base models. This setup allowed linear, tree-based, neural-network, and ensemble architectures to be compared under the same preprocessing, partitioning, and validation conditions.

Hyperparameter tuning was performed internally by `H2O AutoML` under a fixed search budget, rather than through a separate manual grid search. For both predictor configurations, AutoML was run with `max_models = 5`, `max_runtime_secs = 6000 s`, and `seed = 1`. Candidate models were compared using the same 70/30 train/hold-out partition and 5-fold cross-validation protocol, with cross-validated RMSE used as the primary ranking metric. These workflow-level constraints ensured that the baseline and augmented configurations were evaluated under comparable computational and statistical conditions.

Algorithm-specific hyperparameters were explored within the default `H2O AutoML` search space and learner-specific regularization or structural constraints. For GLM, this included internal regularization; for DRF, tree-structure and sampling constraints; for XGBoost, boosting-related settings such as tree depth, learning rate, shrinkage, and regularization; and for deep neural networks, the internal H2O deep-learning search space, including hidden-layer configuration, activation function, regularization, learning-rate settings, and stopping criteria where applicable. These neural-network settings were not manually optimized outside AutoML. No external grid search, manual hyperparameter adjustment, or external feature-selection step was applied after AutoML training. Deep-learning models were included in the candidate pool, but the final top-ranked architectures were selected only according to the common cross-validation criterion.

No additional manual normalization or standardization was applied outside the `H2O AutoML` workflow. Numeric predictors were provided in their physical or derived units after data cleaning, numeric casting, and replacement of non-finite values where required. Learner-specific preprocessing, scaling, and regularization were handled internally by H2O where applicable. This preserved the interpretability of raw seismoelectric variables, engineered attributes, and topographic descriptors while maintaining a common automated benchmarking protocol.

The 70/30 split was chosen based on the size and dependence structure of the modeling dataset rather than as a default convention. The final table contained 437,663 depth-level records, so a 30% hold-out subset retained approximately 131,299 unseen samples, while the 70% training subset provided approximately 306,364 samples for model fitting and 5-fold cross-validation. This balance was considered appropriate because samples are nested within station profiles and are not fully independent along depth. A relatively large hold-out subset was therefore retained to obtain a stable external reference across heterogeneous profile intervals, while cross-validation within the training subset remained the primary basis for model comparison.

The $R^2 \geq 0.70$ requirement was used as a minimum screening criterion rather than as stand-alone proof of model validity. The threshold was adapted from hydrological model-evaluation practice, where R^2 values around or above 0.70 have been considered satisfactory for field-scale flow simulations when interpreted with other performance measures (Moriasi et al., 2015, 2007). Because R^2 alone may be insensitive to bias, scale errors, and outliers (Legates and McCabe Jr., 1999), model acceptance also required RMSE improvement relative to the baseline configuration, lower MAE, consistent cross-validation behavior, preservation of the main hydrostratigraphic transitions, and agreement with the independent hydrogeological appraisal.

Beyond cross-validation statistics, model behavior was examined against an independent validation sector in the Ñuble region and through post-prediction hydrogeological appraisal, following validation logic used in spatially structured hydrogeophysical studies (Oldenborger and Paradis, 2023; Tilahun and Korus, 2023). This combined protocol was intended to evaluate not only numerical accuracy, but also whether the predicted $K_v(z)$ profiles remained hydrogeologically plausible under independent field evidence.

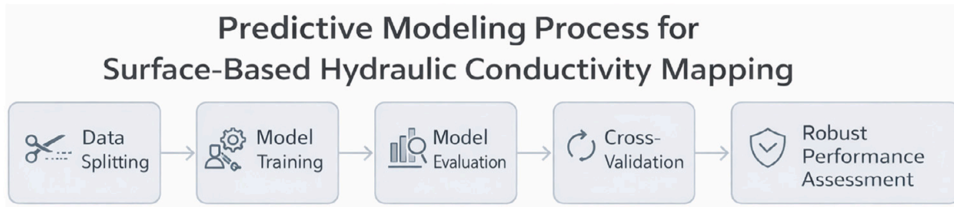

Fig. 5. Schematic overview of the predictive modeling workflow used for model-performance assessment. The figure summarizes data partitioning, model training, internal cross-validation, model comparison, and external robustness assessment under a common modeling protocol. Performance uncertainty was evaluated through the comparison between training, cross-validation, and hold-out validation metrics rather than through pointwise confidence intervals. Formal prediction intervals for individual $K_v(z)$ profiles were not estimated in this study and are identified as a priority for future uncertainty quantification.

2.6. Reference benchmarking and expert validation

Reliable reference information for K_v was established through a collaborative validation framework involving G-Strata, a geophysical consultancy with more than 15 years of experience in groundwater prospecting and hydrogeological diagnosis in the Ñuble Region. To limit circularity, the workflow was organized as a sequential procedure separating target generation, predictor assembly, model fitting, and external validation. First, G-Strata generated the supervisory target `HydCon(Z)` from the raw seismoelectric field records using its standard hydrogeophysical interpretation procedure, before any machine-learning model was trained. Second, the modeling database was assembled by linking this pre-existing target to co-located predictors, including depth, raw dual-channel voltage amplitudes, spatial descriptors, topographic variables, and physically guided signal attributes. Third, supervised regression models were trained to approximate `HydCon(Z)` from the predictor matrix. Fourth, lithostratigraphic logs, post-drilling hydraulic evidence, and structured expert appraisal were used only after prediction to assess physical plausibility and external consistency. In this design, `HydCon(Z)` served only as the response variable and was not included among the predictors. Drilling information was excluded from model training and feature engineering, so the external validation assessed consistency with independent geological and hydraulic evidence rather than with information already used during model fitting (e.g., Shepley, 2024; Oldenborger and Paradis, 2023).

The external benchmark combined regional and site-specific evidence. At the regional scale, previously mapped geological units and prior interpretations of the basin sedimentary architecture provided the geomorphological and depositional context for the Itata–Ñuble alluvial system. At the site scale, lithostratigraphic columns were newly derived from borehole drilling logs at the validation sites and used after model prediction to assess whether the reconstructed K_v profiles were hydrostratigraphically plausible. These local columns were not used during feature engineering, model fitting, or hyperparameter selection. The benchmark also included complementary geophysical assessments routinely used by G-Strata during groundwater exploration. Together, these materials provided an expert-constrained description of the main subsurface units, their vertical arrangement, and the expected hydraulic contrasts among coarse-grained, mixed, and fine-grained intervals.

Lithostratigraphy was not treated as a direct pointwise measurement of continuous K_v, but as independent evidence for hydrostratigraphic plausibility. The comparison focused on whether the predicted conductivity structure reproduced the main site organization, including the depth and thickness of principal intervals, the position of major transitions between contrasting units, and the relative conductivity ranges expected for the interpreted lithological classes. Agreement was evaluated in terms of stratigraphic correspondence and hydrogeological consistency rather than exact depth-by-depth equality. In this context, main vertical contrasts refer to persistent high- and low-K_v intervals and abrupt conductivity transitions associated with major hydrostratigraphic boundaries, rather than isolated pointwise fluctuations. Fidelity was assessed through the joint agreement between predicted and reference profile morphology, preservation of the depth position and thickness of major intervals, cross-validation error metrics, and the physical-plausibility criteria summarized in Table 1.

The expert review was conducted as a structured hydrogeological appraisal rather than as an informal visual inspection. Predicted K_v profiles were reviewed together with independent lithostratigraphic logs, interpreted hydrostratigraphic units, geomorphological context, and post-drilling hydraulic evidence where available. Reviewers assessed each profile using five criteria: hydrostratigraphic ordering, transition-depth consistency, conductivity-range plausibility, productive-interval agreement, and realistic profile morphology (Table 1). The review focused on whether predicted high- and low-conductivity intervals were hydrogeologically coherent, whether major transitions occurred at plausible depths, and whether the profiles contained unrealistic oscillatory artifacts or excessive smoothing. Disagreements were resolved by prioritizing independent field evidence and by treating expert review as a plausibility screen rather than as a source of additional training data. No model parameters were adjusted after expert assessment.

Fig. 6 summarizes the validation chain, from raw field potentials to interpreted seismoelectric conductivity signatures, followed by comparison with stratigraphic logs, pre-drilling predictive assessment, and post-drilling hydraulic evidence.

Additional external support came from post-prediction drilling at the validation site. The completed borehole yielded 62 L/s, which lies within the forecast interval of 45 L/s to 68.4 L/s derived from the hydrogeological interpretation. The midpoint of that interval is 56.7 L/s, giving a difference of about 9.3% relative to the observed yield. This comparison should not be read as a direct prediction of discharge, since borehole yield also depends on screen length, aquifer geometry, well efficiency, and operational factors that are not constrained by the seismoelectric survey alone (cf. Shepley, 2024). Even so, the agreement between the forecast interval and measured yield supports the interpretation that the predicted K_v structure captured the main productive aquifer intervals later confirmed by drilling.

To promote transparency and facilitate further work in hydrogeophysical machine learning, the complete Ñuble Region dataset, including raw voltage traces, interpreted conductivity profiles, and drilling logs, is publicly available in the Zenodo repository (https://doi.org/10.5281/zenodo.17234793).

2.7. Comparative positioning

The proposed workflow occupies an intermediate scale between localized hydraulic testing and conventional geophysical imaging. Pumping and slug tests provide direct hydraulic information but remain spatially sparse and costly to densify at basin scale. ERT and IP offer broader spatial coverage, but their relation to hydraulic conductivity is indirect and depends on petrophysical assumptions, calibration data, and inversion regularization (Koch et al., 2011; Friedel, 2003; Oldenborger and Paradis, 2023). Conventional seismoelectric methods provide a physical link to electrokinetic processes related to permeability, porosity, and saturation, but field signals are commonly noisy and difficult to convert into quantitative K_v profiles without additional processing and validation.

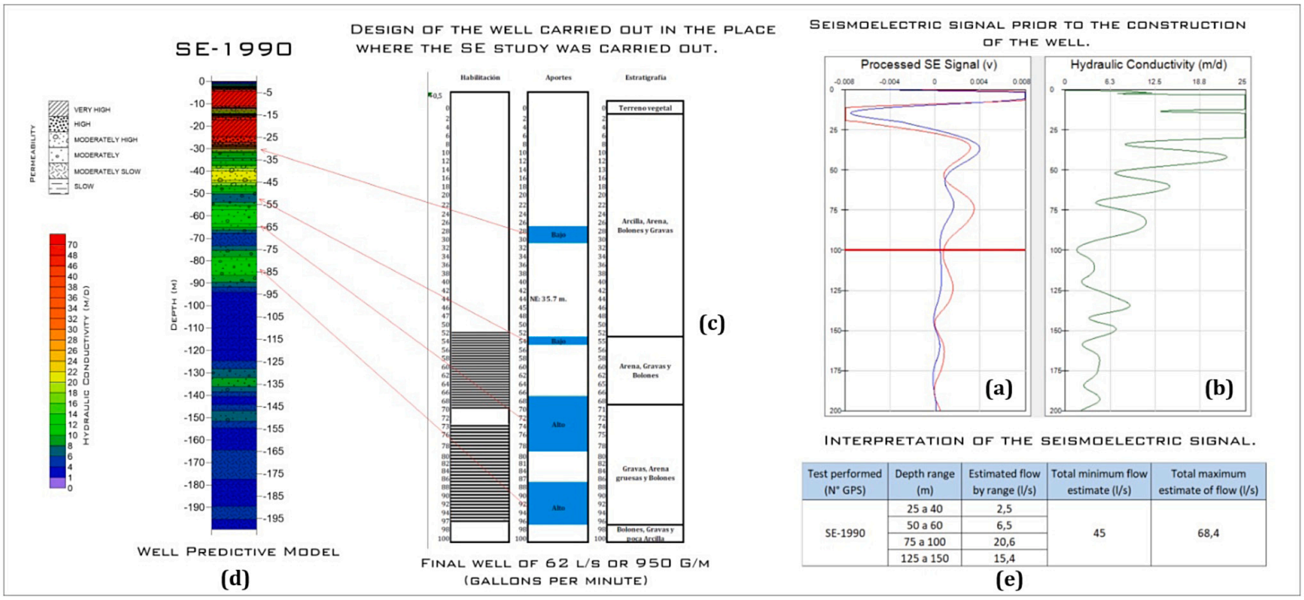

Fig. 6. Expert validation framework integrating seismoelectric predictions, lithostratigraphic information, and post-drilling hydraulic evidence. The diagram separates target generation, supervised model prediction, independent lithostratigraphic comparison, and post-drilling verification. This sequence clarifies that borehole logs and hydraulic evidence were used after prediction as external validation information, not as training inputs. Data provided by G-Strata.

Table 1
Criteria used during expert review to assess the physical plausibility of predicted K_v profiles during external validation.

Criterion	Evaluation basis	Interpretation
Hydrostratigraphic ordering	Comparison between predicted K_v contrasts and the expected hydraulic behavior of coarse, mixed, and fine-grained intervals.	Higher K_v should coincide with more permeable units, whereas lower K_v should coincide with finer or less connected intervals.
Transition-depth consistency	Comparison of the depth and thickness of major high- and low-conductivity intervals with the independent stratigraphic interpretation.	A plausible profile should preserve the position of major vertical transitions rather than reproduce exact pointwise values.
Conductivity-range plausibility	Comparison of predicted K_v magnitudes with values expected for comparable alluvial aquifer materials and local hydrogeological interpretation.	Predicted values should remain within physically reasonable ranges for the interpreted aquifer setting.
Productive-interval agreement	Comparison between predicted high K_v intervals and post-drilling hydraulic evidence, including measured borehole yield.	A plausible profile should identify intervals consistent with later confirmed productive zones.
Profile morphology	Inspection of vertical continuity, abrupt contrasts, and absence of physically implausible oscillatory artifacts.	Profiles should preserve hydrogeologically meaningful contrasts without excessive smoothing or erratic fluctuations.

The present workflow differs from these approaches in three main respects: (1) it exploits electrokinetic responses physically linked to pore-fluid motion and permeability-related processes (Pride, 1994; Grobbe et al., 2020; Hu et al., 2023), rather than relying only on static electrical contrasts; (2) it uses drilling information only for external validation, not for model development; and (3) it evaluates performance against both an explicit baseline and an independent hydrostratigraphic benchmark, following the criteria described in Sections 2.5 and 2.6. Table 2 summarizes this positioning.

3. Results

Models augmented with engineered signal features and topographic descriptors achieved substantially better predictive performance than the baseline configuration. Here, the baseline refers to the model using only raw dual-channel seismoelectric amplitudes and measurement depth as predictors, without engineered signal attributes or topographic descriptors. Based on the cross-validation metrics of the selected stacked ensemble in each configuration, the augmented model increased R^2 from 0.711 to 0.968, reduced RMSE from 3.534 to 1.305 m/d (63.1%), and reduced MAE from 1.368 to 0.546 m/d (60.1%). These results suggest that the augmented predictor space captures relevant information not contained in raw voltage and depth alone. The detailed comparative results are presented in Sections 3.1 and 3.2, with full model statistics reported in Tables 3–7.

3.1. Baseline performance: Voltage and depth configuration

The predictive performance of the candidate models developed under the baseline configuration, using only raw dual-channel voltage and depth as predictors, is summarized in Table 3. Root Mean Square Error (RMSE) was used as the primary ranking criterion because it penalizes large deviations more strongly than average-error metrics and therefore provides a stringent measure of predictive performance in heterogeneous hydrogeophysical settings.

The leaderboard shows that stacked ensemble architectures achieved the best predictive performance under the baseline configuration, slightly outperforming the distributed random forest and clearly exceeding the XGBoost variants. This result suggests that combining learners with different functional assumptions improves robustness

Table 2
Positioning of the proposed seismoelectric workflow relative to common approaches for K_v characterization.

Approach	Main strength	Main limitation for K_v mapping
Pumping and slug tests	Direct hydraulic information at wells or screened intervals.	Spatially sparse; vertical extrapolation away from the tested interval is limited.
ERT/IP	Non-invasive spatial imaging of subsurface electrical contrasts.	Hydraulic interpretation is indirect; depends on petrophysical assumptions and inversion regularization.
Conventional seismoelectric methods	Physical link to electrokinetic processes related to permeability, porosity, and saturation.	Field signals are commonly noisy; quantitative K_v conversion requires additional processing and validation.
Proposed workflow	Surface acquisition with signal conditioning, electrokinetically guided features, supervised regression, and independent validation without drilling input during training.	Transferability to other geological settings requires further testing.

Table 3
Leaderboard of the top-performing regression models using baseline predictors (voltage and depth).

Rank	Model architecture	RMSE	MAE	Train time (s)
1	Stacked ensemble (All)	3.534	1.368	1.91
2	Stacked ensemble (Best)	3.534	1.368	1.92
3	Distributed random forest	3.597	1.392	10.99
4	XGBoost (v1)	4.595	2.044	5.89
5	XGBoost (v2)	4.645	2.087	4.24

Table 4
Statistical performance metrics for the optimal baseline ensemble. Overfitting ratios represent the quotient of Cross-Validation to Training error.

Metric	Training	Cross-Validation	Ratio (CV/Train)
R^2	0.9211	0.7109	–
RMSE (m/d)	1.8054	3.5340	1.96
MAE (m/d)	0.9017	1.3680	1.52

even when the predictor space is restricted to raw amplitudes and depth.

A more detailed summary of the selected baseline ensemble is provided in Table 4. The comparison between training and cross-validation metrics indicates a clear loss of performance from fitting to validation, with RMSE increasing from 1.805 to 3.534 m/d and MAE from 0.902 to 1.368 m/d. Although the baseline model retains moderate explanatory power under cross-validation ($R^2 = 0.711$), these results indicate that the voltage-plus-depth configuration captures only part of the variability represented in the reference conductivity profiles.

These results establish the baseline model as a useful reference for evaluating the contribution of engineered signal features and topographic context in the augmented configuration presented in Section 3.2. In practical terms, the baseline confirms that depth and raw seismoelectric amplitudes already contain predictive information, but also that this information alone is insufficient to reproduce the full conductivity structure with the level of detail required for robust hydrostratigraphic interpretation.

3.1.1. Interpretability analysis: SHAP-based feature attribution

To examine how the optimal baseline model distributes predictive importance across its inputs, we performed an interpretability analysis using SHAP (Shapley Additive exPlanations) values. The results identify depth as the dominant predictor in the baseline architecture (Fig. 7), which is consistent with the strong vertical organization of hydraulic properties in stratified aquifer systems (cf. Shepley, 2024).

The predominance of depth is consistent with the multilayered character of the Central Chile alluvial basins, where hydraulic conductivity is strongly influenced by vertical facies transitions. Although the raw RED and BLUE voltage channels show lower global importance than depth, their SHAP distributions still reveal non-negligible contributions. In particular, their dispersion increases in intervals associated with stronger signal variations, suggesting that they capture localized electrokinetic responses linked to permeability contrasts that depth alone cannot resolve (e.g., Oldenborger and Paradis, 2023; Hu et al., 2023).

This hierarchical predictor structure is also consistent with broader hydrogeophysical and geo-electromagnetic studies showing that raw measurements often retain relevant subsurface information, but that their predictive value is limited when used without contextual or derived descriptors (Huang et al., 2025). In this sense, the baseline SHAP analysis provides an important reference point for the augmented model discussed in Section 3.2: it shows that the predictive signal is real, but largely dominated by vertical position, leaving substantial room for improvement through engineered attributes that better encode inter-channel relationships and local hydrogeophysical structure (cf. Ahmadisharaf et al., 2024; Fan et al., 2025).

Table 5
Predictive ranking for AutoML architectures utilizing consolidated predictors (voltage, depth, and complementary attributes).

Rank	Model architecture	RMSE	MAE	Train time (s)
1	Stacked ensemble (All)	0.951	0.425	3.54
2	Stacked ensemble (Best)	1.031	0.489	3.78
3	XGBoost (v1)	1.101	0.460	52.65
4	XGBoost (v2)	1.126	0.471	67.65
5	Distributed random forest	1.409	0.651	26.26

3.2. Augmented modeling: Integration of topographic and engineered attributes

Models augmented with engineered signal features and topographic descriptors showed a clear improvement over the baseline voltage-plus-depth configuration. In particular, the inclusion of elevation-derived predictors together with nonlinear inter-channel attributes improved predictive performance under the same validation framework used for the baseline models.

Table 5 summarizes the AutoML leaderboard for the augmented predictor set. The best-ranked candidates were stacked ensembles, followed by XGBoost and distributed random forest models, indicating that hybrid architectures were again the most effective under this configuration.

For consistency, the formal comparison with the baseline model is based on the cross-validation metrics of the selected stacked ensemble in each configuration rather than on the leaderboard alone. Under this criterion, the augmented configuration reduced the cross-validated RMSE from 3.534 to 1.305 m/d and the cross-validated MAE from 1.368 to 0.546 m/d, while increasing the cross-validated coefficient of determination from 0.711 to 0.968. These results indicate that the additional predictors provide information that is not captured by raw voltage and depth alone.

The detailed training and cross-validation statistics of the selected enhanced ensemble are reported in Table 6. As expected, prediction error increases from training to cross-validation. Although the validation metrics remain strong, this gap indicates that some generalization risk persists.

This behavior is consistent with the dependence structure of the dataset, where depth-level samples are nested within station profiles and therefore do not represent fully independent observations. Accordingly, model performance should be interpreted primarily as evidence

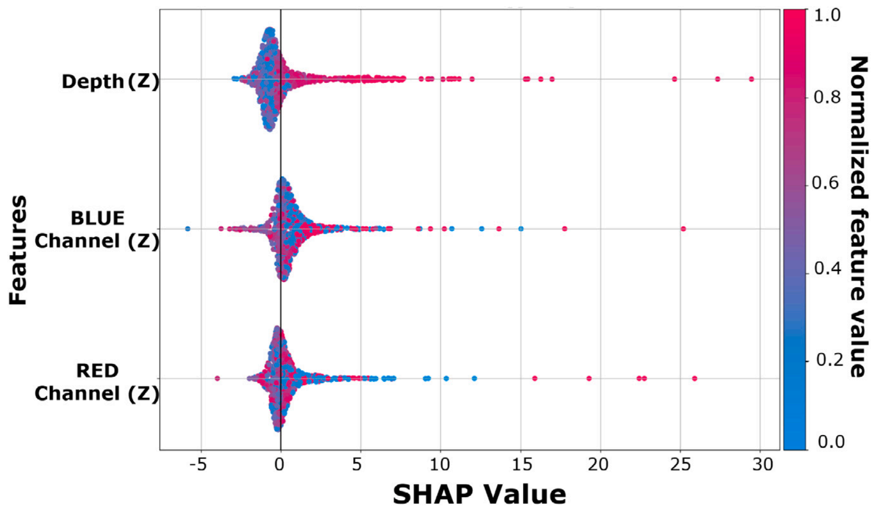

Fig. 7. SHAP-based feature attribution for the baseline architecture. The distribution highlights the dominant role of depth-related structure and the secondary contributions of the raw seismoelectric voltage channels in resolving localized K_v variability.

Table 6
Comparative performance statistics for the optimal enhanced ensemble. Convergence ratios represent the quotient of Cross-Validation to Training error.

Metric	Training	Cross-Validation	Ratio (CV/Train)
R^2	0.9953	0.9682	–
RMSE (m/d)	0.4927	1.3052	2.65
MAE (m/d)	0.3146	0.5464	1.74

Table 7
Summary of the main validation metrics for the selected baseline and augmented modeling configurations. Baseline: raw voltage and depth only. Augmented: voltage, depth, engineered features, and topographic descriptors. Cross-validation metrics correspond to the selected stacked ensemble in each configuration.

Configuration	$RMSE_{train}$	$RMSE_{CV}$	MAE_{CV}	R^2_{CV}	RMSE reduction
Baseline	1.805	3.534	1.368	0.711	–
Augmented	0.493	1.305	0.546	0.968	63.1%

of strong predictive capacity within the surveyed domain rather than as proof of unrestricted transferability.

The improvement is also consistent with the structure of the augmented predictor space. In addition to depth and raw dual-channel amplitudes, the enhanced model incorporates topographic descriptors such as absolute elevation (`Cota`) and relative elevation contrast (`cotadiff`), as well as engineered signal attributes derived from the interaction between channels A and B. These variables provide contextual and nonlinear information that helps differentiate similar seismoelectric responses observed under distinct geomorphological settings. Their contribution is consistent with the hydrogeophysical rationale developed in Section 2.4, where the predictor set was designed to retain interpretable relations between signal structure and hydraulic behavior.

To facilitate comparison between the main modeling configurations, Table 7 consolidates the principal validation metrics for the selected baseline and augmented ensembles. The summary shows that the performance gain is substantial and systematic across the main error indicators, supporting the value of combining engineered signal descriptors with topographic context in the estimation of K_v.

A profile-level comparison for validation points 1197 and 1199 further illustrates the effect of predictor augmentation (Fig. 8). Relative to the baseline model, the augmented configuration better preserves the depth position, thickness, and amplitude contrast of the dominant high- and low-K_v intervals, showing improved agreement with the expert-interpreted reference profiles. In particular, the enhanced model better preserves abrupt transitions between conductive and less conductive intervals, which is relevant from a hydrostratigraphic perspective because these transitions control vertical connectivity and aquifer compartmentalization.

Although Fig. 8 does not display individual predictors, it provides indirect evidence that the additional attributes contribute useful information to the final reconstruction. The gain is expressed not only in lower prediction error, but also in a profile morphology that is more consistent with the benchmark conductivity structure. This distinction is important because, in hydrogeophysical applications, acceptable numerical accuracy alone does not guarantee that the reconstructed vertical organization remains geologically plausible.

To interpret the behavior of the enhanced ensemble, SHAP (Shapley Additive exPlanations) values were analyzed at the global and local levels. At the global level, mean absolute SHAP values identify depth as one of the dominant predictors, but they also highlight the importance of engineered attributes such as `dA`, `dB`, `A*B`, and the topographic contrast `cotadiff` (Fig. 9). This pattern indicates that the model does not rely only on vertical position or raw amplitudes, but also incorporates signal interactions and geomorphological context.

At the local level, SHAP values quantify the signed contribution of each predictor to an individual estimate at a given depth and station. These local attributions do not constitute direct lithological identification, but they help determine whether a prediction is driven primarily by depth, by cross-channel signal structure, or by topographic setting. Taken together, the coherence between the global ranking and the local contributions supports the internal consistency of the enhanced model and strengthens the interpretation that the added predictors capture relevant aspects of the seismoelectric response.

The sensitivity of the augmented configuration is also evident from the contrast with the baseline model. The marked improvement in validation metrics indicates that prediction quality depends on the inclusion of engineered attributes and topographic descriptors rather than on depth and raw voltages alone. At the feature level, the SHAP ranking suggests that this gain is distributed across several predictor groups, particularly depth, first-difference attributes (`dA`, `dB`), cross-channel interactions (e.g., `A*B`), and topographic context (`cotadiff`). This pattern suggests that the enhanced ensemble benefits from the combined contribution of multiple physically motivated variables rather than from dependence on a single dominant engineered predictor.

To complement this interpretability analysis, direct association metrics were computed between selected signal-derived attributes and the reference `HydCon(Z)` profile. Among the evaluated variables, the

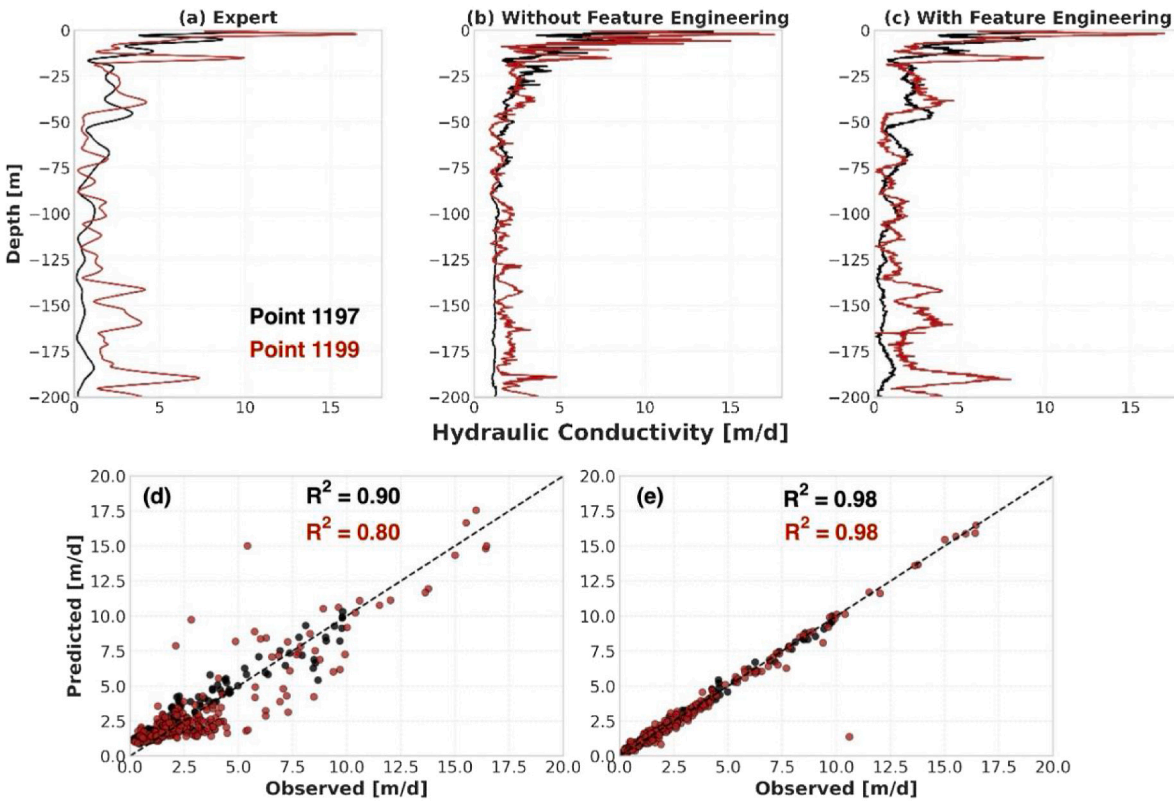

Fig. 8. Validation comparison of vertical K_v profiles for measurement points 1197 and 1199. Panel (a) shows the expert-interpreted reference profiles used as the hydrostratigraphic benchmark. Panel (b) shows predictions from the baseline model using raw voltages and depth only, illustrating reduced ability to reproduce sharp vertical contrasts. Panel (c) shows predictions from the augmented model including engineered signal attributes and topographic descriptors, the augmented model reproduced the main vertical contrasts more faithfully than the baseline configuration. Panels (d) and (e) present the corresponding observed–predicted relationships for the baseline and augmented configurations, respectively; the tighter clustering around the 1:1 line and the higher R^2 values in panel (e) indicate the improved predictive agreement achieved by feature augmentation.

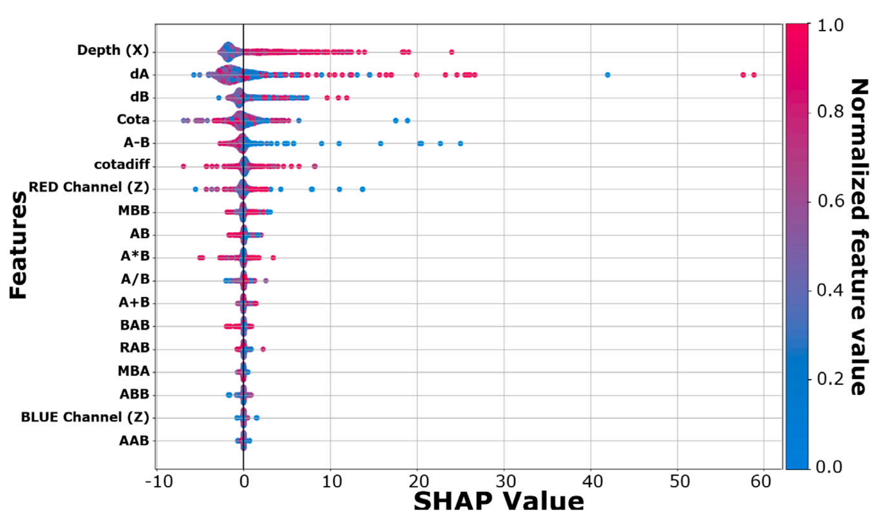

Fig. 9. Global feature attribution (SHAP) for the enhanced ensemble, illustrating the role of non-linear signal interactions and topographic context in refining K_v estimates.

Table 8
Parameter settings and tuning criteria used for profile-level post-processing filters applied to predicted K_v profiles.

Filter	Parameters	Purpose	Tuning criterion
Savitzky–Golay	Window length = 35 samples; polynomial order = 4; mode = `nearest`. Tested window lengths = 20–40 samples and polynomial orders = 2–4.	Local smoothing while preserving peaks and steep vertical gradients.	Selected because it reduced short-wavelength oscillations without shifting the main conductivity transitions along depth or suppressing local extrema.
Wavelet low-pass	Mother wavelet = `db4`; level = 4; approximation-only reconstruction after detail removal. Tested families: `haar`, `db2`, `db4`, `sym4`, `sym8`, `coif1`, `bior3.5`, `rbio3.1`, and `dmey`.	Multi-scale denoising and low-pass smoothing.	Retained because it provided effective multi-scale smoothing while preserving the principal hydrostratigraphic contrasts and avoiding excessive flattening of sharp vertical changes.
FFT low-pass	Cutoff ratio = 0.01 of signal length; coefficients outside the retained low-frequency band set to zero before inverse transform.	Removal of high-frequency fluctuations.	Evaluated as a frequency-domain alternative; retained for comparison, but not preferred when it attenuated abrupt vertical contrasts or introduced excessive profile smoothing.
Notch	Center frequency = 50 Hz; quality factor = 30.	Suppression of narrow-band power-line interference.	Applied only to attenuate known electrical interference when present, while preserving broader profile-scale trends.
Butterworth	Order = 1–3; cutoff frequency = 35–150.	Smooth low-pass filtering with monotonic attenuation.	Evaluated across order and cutoff combinations to reduce profile roughness while avoiding excessive attenuation of hydrostratigraphic transitions.
Chebyshev	Order = 1–3; cutoff frequency = 35–170; passband ripple = 0.1 dB.	Sharper spectral attenuation than Butterworth filtering.	Evaluated as a sharper low-pass alternative; not preferred when passband ripple or stronger attenuation introduced visible profile distortion.

cross-channel interaction term `A*B` showed the clearest relationship, with Pearson and Spearman correlation coefficients of 0.224 and 0.233, respectively. Although these associations are moderate, they indicate that some engineered seismoelectric attributes retain direct statistical information related to the target hydraulic property. Considered together with the multivariate performance of the enhanced ensemble, these results support the use of seismoelectric signal interactions as informative indirect predictors of vertical hydraulic conductivity.

3.3. Effect of filtering and post-processing on seismoelectric model outputs

To complement the predictive comparison (Sections 3.1 and 3.2), we evaluated profile-level post-processing to determine whether smoothing could reduce short-wavelength oscillations while preserving the main hydrostratigraphic structure of the predicted K_v profiles. Because this analysis was performed after model inference, it should be interpreted as an assessment of structural preservation and visual continuity rather than predictive skill.

The parameter settings adopted for each filtering method are summarized in Table 8. Using these settings, Figs. 10 and 12 compare the filtered profiles obtained with Savitzky–Golay smoothing, wavelet low-pass filtering, FFT low-pass filtering, notch filtering, and Butterworth and Chebyshev digital filters for validation points 1197 and 1199, respectively.

For validation point 1197, the filtered profiles show different trade-offs between noise reduction and preservation of sharp vertical contrasts (Fig. 10). Savitzky–Golay and wavelet filtering provided the most balanced reconstructions, reducing local oscillations while retaining the main conductive intervals and abrupt transitions. In contrast, stronger low-pass alternatives tended to smooth parts of the vertical structure more aggressively.

This behavior is consistent with the corresponding scatter plots against the original model output (Fig. 11), where methods that remain closer to the 1:1 line preserve the original profile structure more closely. In this context, the reported R^2 values should be interpreted as indicators of structural similarity to the unfiltered prediction rather than as independent validation metrics.

For validation point 1199, the same general pattern is observed. Savitzky–Golay and wavelet filtering again provide reconstructions that preserve key vertical variations while reducing local roughness, whereas the more aggressive frequency-domain alternatives produce smoother profiles at the cost of attenuating some sharp transitions (Fig. 12).

The corresponding scatter plots (Fig. 13) support the same interpretation, showing that filters with stronger smoothing depart more from the original prediction, whereas Savitzky–Golay and wavelet filtering better preserve the predicted conductivity architecture.

Taken together, these comparisons indicate that Savitzky–Golay and wavelet filtering provide the most favorable balance between smoothing and structural preservation among the post-processing methods evaluated. Their effect is expressed mainly as improved profile continuity and reduced small-scale oscillation, while maintaining the principal conductivity contrasts identified by the enhanced model. These results support their use as visualization-oriented post-processing tools, but they should not be interpreted as evidence of improved predictive accuracy relative to an external hydrogeological benchmark.

4. Discussion

4.1. Performance dynamics of the automl framework

The superior performance of the stacked ensembles in both the baseline and augmented configurations is consistent with previous groundwater-related prediction studies where hybrid or ensemble strategies outperformed single-model approaches (Trabelsi et al., 2022). It is also consistent with the rationale of stacked generalization, which combines learners with different structural assumptions to reduce generalization error (Wolpert, 1992). In this study, the advantage of the stacked ensembles is plausibly explained by the complementarity among the base learners. The GLM component favors smooth and approximately linear trends, whereas DRF and XGBoost capture nonlinear interactions, threshold-like behavior, and local predictor interactions through tree-based partitioning and boosting.

This combination reduces dependence on a single functional form and provides a flexible response to the heterogeneous and nonlinear structure of the seismoelectric predictor space. The empirical rankings reported in Sections 3.1 and 3.2 support this interpretation, as stacked ensembles outperformed the individual candidate architectures under the same validation framework. However, the gap between training and cross-validation errors, particularly in the augmented configuration, indicates that the gain in predictive power should be interpreted together

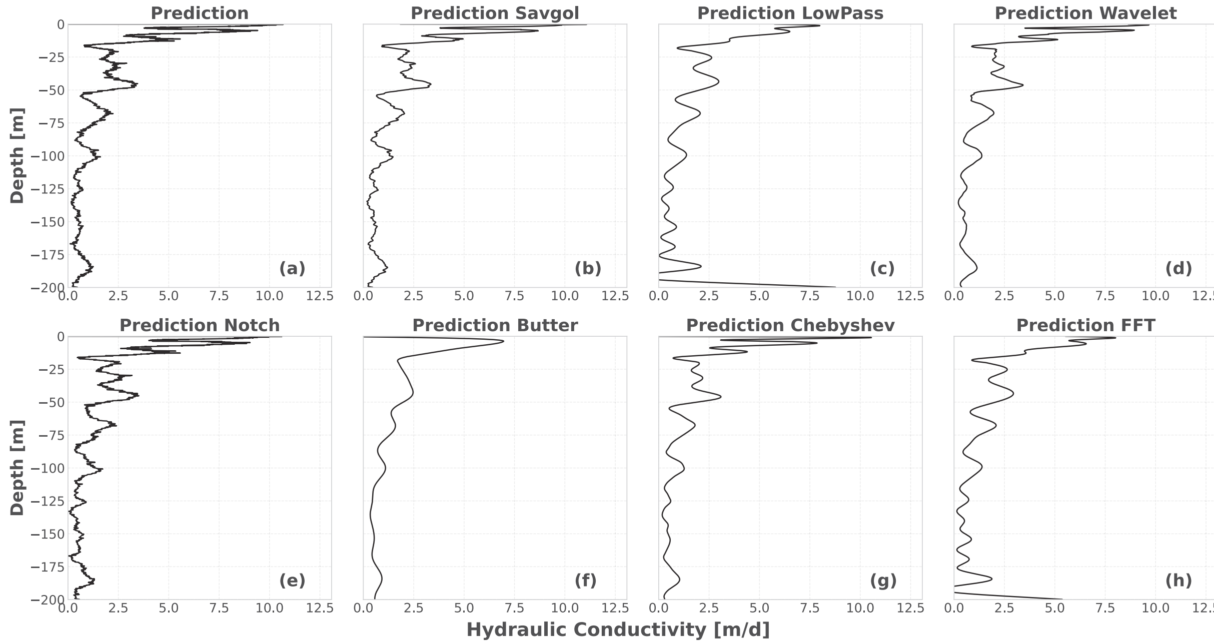

Fig. 10. Effect of post-processing filters on the predicted vertical K_v profile for validation point 1197. Panel (a) shows the original unfiltered prediction. Panels (b)–(h) show the profiles after applying Savitzky–Golay, low-pass, wavelet, notch, Butterworth, Chebyshev, and FFT-based filters, respectively. The comparison highlights the extent to which each method reduces short-wavelength oscillations while preserving the main hydrostratigraphic morphology, particularly sharp vertical transitions and the depth position of major conductive intervals.

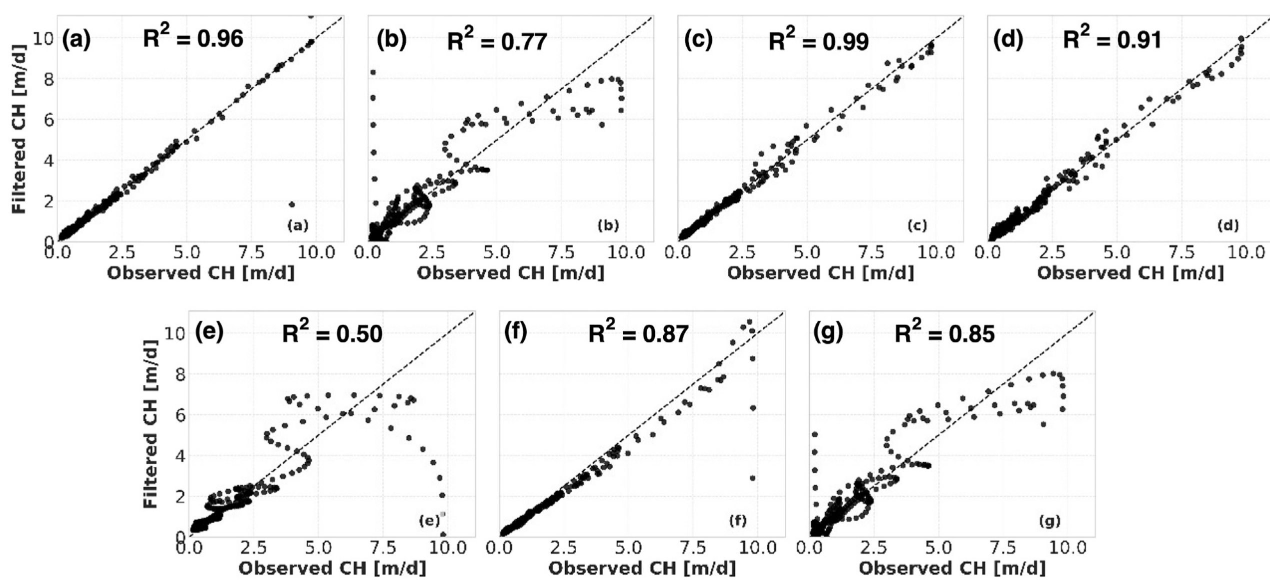

Fig. 11. Scatter plots for post-processed predictions at point 1197, comparing each filtered K_v profile against the original model output. Panels (a)–(g) correspond to Savitzky–Golay, low-pass, wavelet, notch, Butterworth, Chebyshev, and FFT filtering, respectively. The dashed 1:1 line indicates perfect agreement with the unfiltered prediction, whereas the reported R^2 values summarize how strongly each filter preserves the original conductivity structure.

with the dependence structure of the dataset. The results therefore support improved predictive consistency within the surveyed domain, but not unrestricted generalization beyond the sampled hydrogeological setting.

4.2. Geophysical proxies and hydrostratigraphic plausibility

The predicted K_v structure is hydrogeologically relevant insofar as it remains consistent with independent lithostratigraphic expectations, lateral geomorphological organization, and post-drilling verification. As shown by the profile-level comparisons in Section 3.2, the augmented model preserved the dominant high- and low-K_v intervals and the abrupt transitions between them more clearly than the baseline configuration, particularly at validation points 1197 and 1199. This behavior is important because vertical hydraulic contrasts govern connectivity between aquifer layers and the distribution of barriers to vertical exchange (cf. Shepley, 2024). The lithostratigraphic reference used for this comparison combined previously mapped regional geological context with site-specific columns newly derived from validation borehole logs. This distinction is relevant because regional mapping provided depositional context, whereas local columns provided independent post-model evidence for evaluating whether the predicted vertical K_v contrasts were physically plausible.

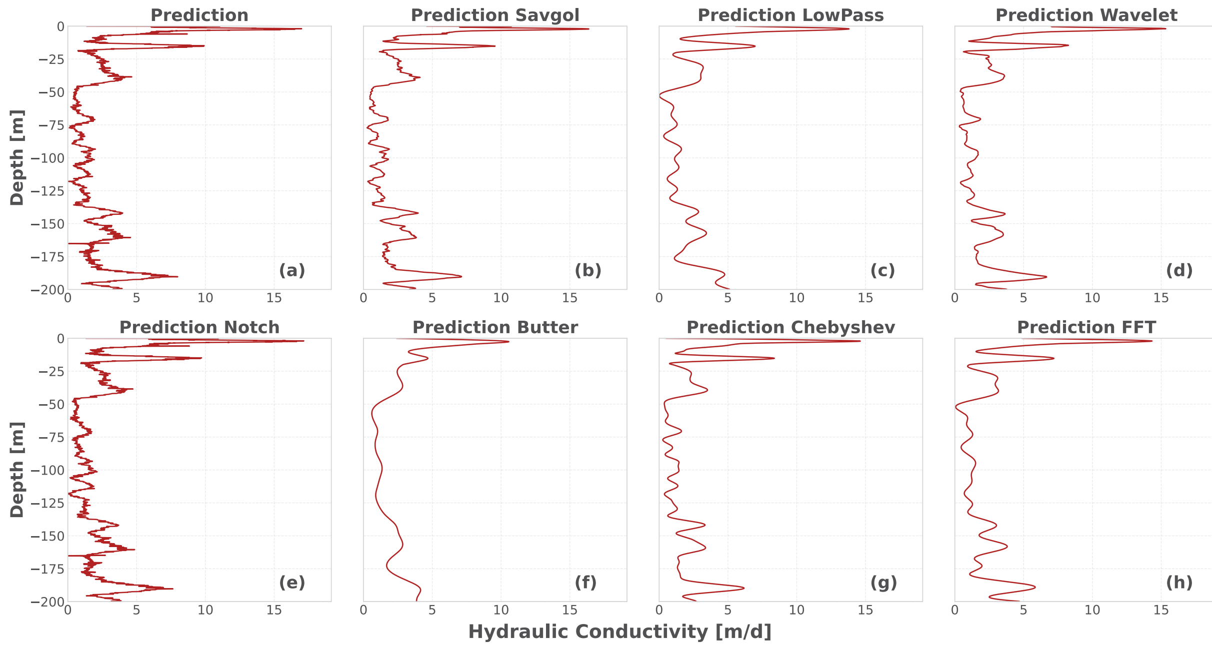

Fig. 12. Effect of post-processing filters on the predicted vertical K_v profile for validation point 1199. Panel (a) shows the original unfiltered prediction. Panels (b)–(h) show the profiles after applying Savitzky–Golay, low-pass, wavelet, notch, Butterworth, Chebyshev, and FFT-based filters, respectively. As in Fig. 10, the comparison highlights the trade-off between noise reduction and preservation of hydrostratigraphically meaningful vertical contrasts.

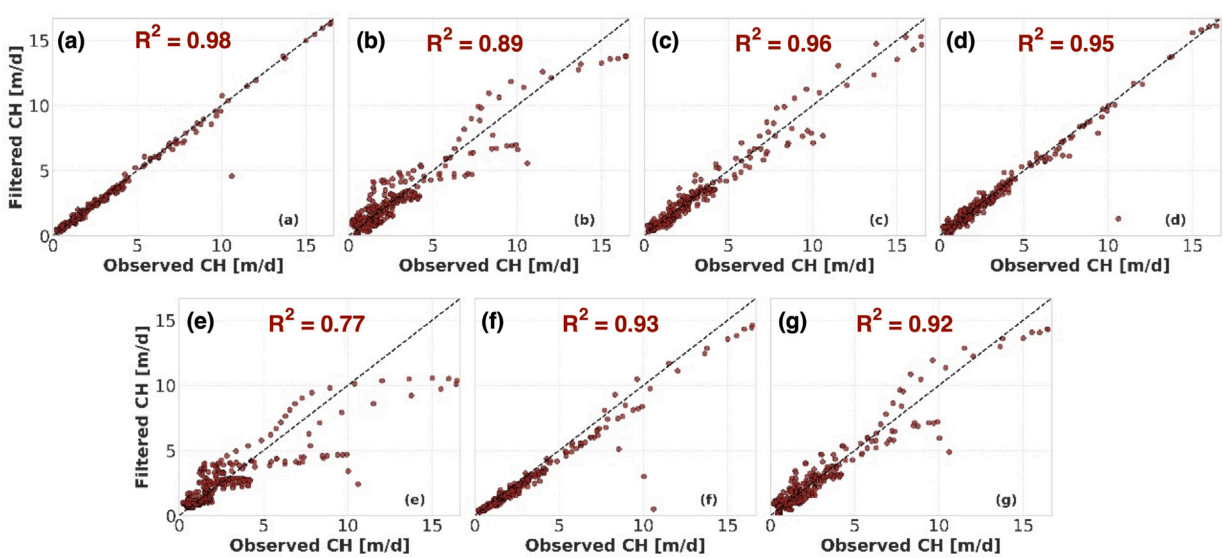

Fig. 13. Scatter plots for post-processed predictions at point 1199, comparing each filtered K_v profile against the original model output. Panels (a)–(g) correspond to Savitzky–Golay, low-pass, wavelet, notch, Butterworth, Chebyshev, and FFT filtering, respectively. The dashed 1:1 line indicates perfect preservation of the original prediction, and the reported R^2 values quantify the structural similarity between filtered and unfiltered profiles.

Within the Itata–Ñuble alluvial system, higher-K_v intervals are consistent with coarse gravelly deposits associated with higher-energy fluvial phases, which likely constitute the main productive aquifer horizons. In contrast, lower-K_v intervals are more consistent with silty-clay interbeds that act as local aquitards, restrict vertical flow, and reduce hydraulic connectivity. The predicted conductivity structure is also laterally coherent in the meridional section shown in Fig. 1d, where the main K_v patterns follow the broader geomorphological organization of the basin rather than appearing spatially erratic. Where available, the verification borehole further supports this interpretation by showing that the main high-conductivity intervals are consistent with coarse units identified at depth.

The overall range of predicted K_v values is compatible with values reported for alluvial aquifers of comparable lithological composition under Mediterranean-climate conditions (Medici and West, 2021; Shepley, 2024). Similar correspondences between data-driven geophysical proxies and hydrostratigraphic organization have been reported in complex alluvial and karst environments (Oldenborger and Paradis, 2023; Medici and West, 2021). These observations indicate that aggregate metrics such as RMSE are informative but not sufficient on their own to assess hydrogeological realism. For this reason, the external appraisal also considered the physical-plausibility criteria defined in Table 1: hydrostratigraphic ordering, transition-depth consistency, conductivity-range plausibility, productive-interval agreement, and realistic profile morphology. These criteria were applied during a structured expert review and were not used to modify model parameters. The appraisal should therefore be interpreted as an additional plausibility check rather than as a post hoc calibration step.

Accordingly, the external validation should be interpreted as a consistency-based hydrogeological appraisal rather than as a point-wise verification of the true K_v field. This distinction is important because the validation data provide independent lithological and hydraulic evidence, but not continuous depth-by-depth measurements of vertical hydraulic conductivity. The agreement between the predicted high-K_v intervals, the independent stratigraphic interpretation, and the post-drilling yield evidence supports the physical plausibility of the reconstructed profiles while recognizing the uncertainty inherent in indirect hydrogeophysical prediction.

4.3. Mechanistic value of multidimensional feature engineering

The contrast between the baseline and augmented configurations highlights the limitations of relying only on raw signal amplitudes and depth. As shown by the SHAP analysis in Section 3.2, the improved performance of the augmented model was not driven by a single added variable, but by the combined contribution of physically motivated predictors, including first-order depth differences, cross-channel interactions, and topographic descriptors. This pattern suggests that the engineered attributes capture aspects of the seismoelectric response that are relevant to hydraulic structure but are not fully represented by raw amplitudes alone.

The contribution of engineered features derived from channels A and B, including products, ratios, and first-order depth differences, is consistent with hydrogeophysical studies emphasizing the value of nonlinear descriptors for revealing latent information in electromagnetic and coupled-field measurements (e.g., Huang et al., 2025; Li et al., 2022). The SHAP summary plot in Fig. 9 provides quantitative evidence of the relative contribution of these predictors. Depth was the most influential variable, followed by first-difference signal attributes, indicating that the model relied strongly on vertical position and abrupt changes in the dual-channel seismoelectric response. Topographic descriptors also contributed measurably: `Cota` ranked fourth and `cotadiff` ranked sixth among all predictors. Their presence among the six most influential variables supports the interpretation that topographic context added useful information beyond raw seismoelectric amplitudes and depth.

The role of these topographic variables should be interpreted as contextual rather than directly hydraulic. `Cota` likely encodes broad geomorphological position within the alluvial system, whereas `cotadiff` captures local relief and elevation gradients that may relate to depositional surface changes, lateral facies organization, and hydrostratigraphic continuity. Therefore, the improvement of the augmented model is attributed to the joint effect of seismoelectric attributes, physically guided feature engineering, and geomorphological context, rather than to topography alone.

At the same time, the engineered variables should not be interpreted as direct one-to-one measurements of hydraulic conductivity. The moderate direct association observed for `A*B` indicates that some seismoelectric-derived attributes contain measurable statistical information related to the reference `HydCon(Z)` profile. Their main predictive value, however, emerges when they are integrated within a multivariate framework. The engineered predictor space is therefore best understood as a structured proxy system that helps translate complex seismoelectric responses into hydraulically meaningful spatial patterns.

4.4. Practical implications and prospective research

Compared with ERT and IP workflows, the proposed approach does not rely primarily on static electrical contrasts or petrophysical calibration to infer K_v. Instead, it uses seismoelectric attributes linked to electrokinetic coupling and evaluates the resulting profiles against an independent hydrostratigraphic benchmark. This distinction is relevant for pre-drilling assessment because the workflow aims to recover vertical hydraulic structure from surface measurements while reserving borehole information for external validation.

Despite the strong performance of the proposed workflow, several limitations and sources of uncertainty should be considered. First, the gap between training and cross-validated error in the augmented model (Table 6), with an RMSE ratio of 2.65, indicates that some generalization risk remains. This behavior is likely related to the dependence among depth samples within individual profiles and to the smaller effective number of independent spatial units than the full sample count suggests. Second, the supervisory target `HydCon(Z)` is an expert-interpreted reference rather than a direct continuous physical measurement of K_v. Systematic assumptions embedded in the interpretation procedure may therefore be partially transferred to the trained model, especially where the seismoelectric signature is ambiguous. The uncertainty of this target was not explicitly quantified.

Potential sampling bias should also be considered. The station layout was spatially irregular and partly constrained by terrain accessibility, land access, and the need to cover the main geomorphological units. As a result, some hydrostratigraphic settings may be more densely represented than others. The depth-level sampling structure further increases the nominal number of records without providing an equivalent number of independent spatial units, which may bias the model towards better-sampled sectors or more common profile types. The train–hold-out partition did not introduce a marked target-distribution imbalance: the training and hold-out subsets showed similar mean `HydCon(Z)` values of 6.188 and 6.109 m/d and median values of 3.356 and 3.344 m/d, respectively. However, the overall target distribution was strongly right-skewed, indicating that low- to moderate-conductivity intervals were more densely represented than rare high-K_v intervals. The model may therefore be better constrained for common conductivity ranges than for extreme high-conductivity zones.

The robustness of the predicted K_v profiles was assessed through complementary checks rather than through full probabilistic uncertainty quantification. Model performance was evaluated using cross-validation and an independent hold-out subset. The comparison between baseline and augmented configurations tested whether the improvement was attributable to the engineered predictor space rather than to the modeling architecture alone. Profile-level post-processing was applied only after model inference to assess whether the predicted vertical patterns remained structurally coherent under controlled smoothing. In addition, the reconstructed profiles were evaluated using the physical-plausibility criteria summarized in Table 1.

The model-performance figure summarizes training, cross-validation, and hold-out metrics, but it should not be interpreted as providing pointwise confidence intervals for predicted $K_v(z)$ profiles. Formal prediction intervals or error bands for individual profiles were not estimated. Future work should address this limitation using bootstrap resampling, repeated spatially grouped cross-validation, independently trained model ensembles, or conformal prediction to generate uncertainty bands around $K_v(z)$ profiles.

Additional support came from the expert validation procedure, in which the predicted K_v profiles were compared with independent lithostratigraphic information, post-drilling hydraulic evidence, and complementary geophysical observations available from the site. Electrical-resistivity measurements acquired in parallel by the expert team were used qualitatively as an additional consistency check on subsurface contrasts. These measurements were not used for model training, feature engineering, or hyperparameter selection, but helped assess whether the main predicted high- and low-conductivity intervals were compatible with independent geophysical indications of material or saturation contrasts. This multi-evidence appraisal reduces the likelihood that the predicted profiles reflect only model-specific artifacts.

Prediction robustness is also conditional on the quality of the initial signal conditioning. Because engineered attributes were derived after time conversion, depth mapping, 50 Hz notch filtering, and MC-SESR normalization, errors in these steps may propagate into the predictor matrix. Inaccurate time-to-depth conversion could shift vertical conductivity contrasts, incomplete suppression of power-line interference could introduce spurious spectral components, and unstable channel amplitudes could affect inter-channel ratios, products, and first differences. Future applications should explicitly test sensitivity to acquisition frequency, notch-filter parameters, time-depth conversion, and MC-SESR stability.

The contextual value of topographic descriptors such as `Cota` and `cotadiff` may vary among sites. These variables contributed measurably within the present alluvial setting, where elevation and local relief are linked to geomorphological organization. However, their value may decrease in low-relief settings, where water-table geometry, depositional surfaces, and geomorphological contrasts are less pronounced. Similarly, transferability to geological settings with different lithological compositions, hydrochemical conditions, or electrokinetic coupling behavior has not yet been tested. The reported performance should therefore be interpreted as evidence of predictive consistency within the surveyed domain rather than as proof of unrestricted transferability.

These limitations define the practical scope of the results. Within the surveyed domain, the workflow provides a useful non-invasive approach for reconstructing field-scale conductivity patterns that are consistent with independent hydrogeological evidence. Broader applicability should be evaluated across contrasting hydrogeological environments, with explicit quantification of uncertainty in the expert-derived target and sensitivity of the learned relationships to site-specific electrokinetic conditions (cf. Fan et al., 2025; Ahmadisharaf et al., 2024). Future uncertainty analyses should also propagate acquisition and preprocessing errors through the feature-engineering pipeline, compare independently trained model ensembles, and generate prediction intervals for $K_v(z)$ profiles. Such analyses would provide a stronger basis for evaluating uncertainty in high-K_v zones, transition depths, and laterally interpolated conductivity sections.

The post-processing analysis presented in Section 3.3 suggests that visualization-oriented smoothing may improve profile continuity, but this should be distinguished from any claim of improved predictive accuracy against an external benchmark. Post-processing filters should therefore be interpreted as tools for structural visualization and profile-level comparison, not as substitutes for external validation or uncertainty quantification.

Future work should also explore how the profile-based workflow can be extended to horizontal hydraulic conductivity (K_h), two-dimensional sections, and three-dimensional mapping. The present study focuses on $K_v(z)$ because the seismoelectric response was organized as depth-resolved station profiles and because vertical contrasts control aquifer layering and barriers to vertical exchange. A natural next step, already being developed from the rapid acquisition of multiple closely spaced stations, is to use conductivity profiles recorded at several points to evaluate effective lateral resolution and construct preliminary two-dimensional sections of hydraulic structure. Estimating K_h would require additional information on lateral gradients, directional connectivity between stations, and independent hydraulic evidence such as pumping or interference tests. Similarly, 2D and 3D mapping would require the integration of neighboring $K_v(z)$ profiles through geostatistical interpolation, spatial machine-learning models, or physics-informed constraints, along with explicit uncertainty propagation and validation against independent boreholes or hydraulic tests.

5. Conclusions

This study examined a workflow for estimating vertical hydraulic conductivity (K_v) from surface-based seismoelectric measurements combined with supervised machine learning. The main novelty is the explicit integration of dual-channel seismoelectric attributes, physically guided inter-channel features, and topographic descriptors for depth-resolved K_v mapping. This differs from hydrogeophysical approaches that rely primarily on direct hydraulic tests, electrical or electromagnetic proxies, or geophysical attributes calibrated with borehole information. In the proposed workflow, borehole data were not used during model development, but were reserved for external hydrostratigraphic validation.

Within the study domain, adding physically informed engineered attributes and topographic descriptors to the raw dual-channel signals led to a clear improvement over the baseline model based only on voltage and depth. Using the cross-validation metrics of the selected stacked ensemble in each case, the augmented configuration increased R^2 from 0.711 to 0.968, reduced RMSE from 3.534 to 1.305 m/d, and reduced MAE from 1.368 to 0.546 m/d.

The improvement was not only numerical. Compared with the baseline configuration, the augmented model better preserved persistent high- and low-K_v intervals, including their depth position and abrupt vertical transitions, and generated profiles that were more consistent with the independent hydrostratigraphic benchmark. SHAP analysis also showed that, although depth remained a dominant predictor, first-difference attributes, cross-channel signal interactions, and topographic descriptors contributed meaningfully to the final estimates. These results indicate that the added predictors captured aspects of subsurface hydraulic structure that were not represented by raw amplitudes alone.

The external validation supports this interpretation. At the validation site, the predicted conductivity structure was consistent with lithostratigraphic expectations and with productive intervals later confirmed by drilling. The measured borehole yield of 62 L/s also fell within the forecast range derived from the hydrogeological interpretation, supporting the physical plausibility of the reconstructed profiles. This agreement should not be interpreted as exact pointwise recovery of the true K_v field, but as evidence that the workflow can recover field-scale conductivity patterns that are hydrogeologically meaningful.

Overall, surface seismoelectric data combined with physically informed feature engineering and supervised learning provide a useful basis for field-scale mapping of vertical hydraulic conductivity in heterogeneous, data-scarce environments. The main remaining challenges are uncertainty in the expert-derived target, sensitivity to signal-conditioning choices, and transferability across contrasting hydrogeological settings. Future work should quantify prediction uncertainty more explicitly and evaluate how the profile-based workflow can be extended towards horizontal hydraulic conductivity (K_h), two-dimensional sections, and three-dimensional hydraulic mapping.

CRediT authorship contribution statement

Roberto Aedo-García: Writing – original draft, Visualization, Validation, Methodology, Investigation, Funding acquisition, Formal analysis, Data curation, Conceptualization. **Jorge Jímenez:** Funding acquisition, Data curation, Conceptualization. **Felipe Quiero:** Methodology. **Miguel Valdebenito:** Funding acquisition, Data curation. **Yamisleydi Salgueiro:** Methodology, Investigation, Formal analysis. **Carlos Rey:** Methodology, Investigation, Formal analysis, Data curation. **Gonzalo S. Saldías:** Writing – original draft, Validation, Investigation, Funding acquisition, Formal analysis, Data curation, Conceptualization.

Declaration of competing interest

The authors declare that they have no known competing financial interests or personal relationships that could have appeared to influence the work reported in this paper.

Table 9
Attributes derived from signals A and B, including their mathematical definition, physical meaning, and expected hydraulic relevance.

Attribute	Expression	Description
Mean	$\frac{A+B}{2}$	Central tendency of the two channels; reduces short-scale noise and emphasizes the common-mode response. It helps represent broad depth trends associated with persistent permeable or low-permeability intervals.
Difference	$A - B$	Highlights signed channel asymmetry and local anomalies. This contrast helps detect channel-dependent departures that may reflect vertical or lateral changes in subsurface hydraulic structure.
Product	$A \cdot B$	Encodes nonlinear channel interaction and emphasizes coupled variations when both signals respond coherently. It captures nonlinear behavior expected in heterogeneous media where permeability, saturation, and pore connectivity interact.
Ratio	$\frac{A}{B}$	Captures proportional channel changes and relative scaling. It helps identify intervals where one channel changes more strongly than the other, potentially indicating permeable transitions.
Absolute difference	$\lvert A - B \rvert$	Measures channel discrepancy independently of sign. It provides a robust indicator of inter-channel asymmetry and supports identification of zones where the two-channel response diverges near hydraulic or lithological transitions.
Quadratic difference	$A^2 - B^2$	Nonlinear contrast that amplifies magnitude differences at higher amplitudes. It represents nonlinear signal behavior typical of complex terrains, where subtle channel differences may become informative near strong subsurface contrasts.
Quadratic sum	$A^2 + B^2$	Energy-like magnitude proxy combining both channels. It summarizes joint signal strength and may help distinguish intervals with stronger seismoelectric response associated with hydraulic-connectivity or material contrasts.
Root quadratic difference	$\sqrt{\lvert A^2 - B^2 \rvert}$	Scaled nonlinear contrast that stabilizes large quadratic differences while retaining sensitivity to channel imbalance. It captures nonlinear inter-channel differences without allowing extreme amplitudes to dominate.
Moving average A	$MA_t = \frac{1}{2}\sum_{i=0}^{1} A_{t-i}$	Short-window local average of channel A; reduces acquisition-scale fluctuations while preserving local depth trends. It helps represent gradual changes associated with broader subsurface intervals.
Moving average B	$MB_t = \frac{1}{2}\sum_{i=0}^{1} B_{t-i}$	Short-window local average of channel B; reduces acquisition-scale fluctuations while preserving local depth trends. Together with MA_t, it supports comparison of smoothed channel behavior across depth.
First difference A	$A_t - A_{t-1}$	Captures abrupt vertical changes and local slope variations in channel A. This is important for identifying intervals where the signal changes rapidly, potentially marking transitions between permeable and less permeable structures.
First difference B	$B_t - B_{t-1}$	Captures abrupt vertical changes and local slope variations in channel B. It complements dA by identifying channel-specific slope changes related to hydrostratigraphic boundaries or localized permeability changes.
Asymmetric mix A+B^2	$A + B^2$	Combines linear channel A with nonlinear amplification of channel B. It represents asymmetric channel behavior and nonlinear responses that may arise in heterogeneous subsurface conditions.
Asymmetric mix A−B^2	$A - B^2$	Combines linear channel A with a nonlinear penalty from channel B. It encodes regimes where one channel dominates or diverges, supporting detection of permeable-structure changes and complex signal-capture conditions.

Acknowledgments

This study was financially supported by G-Strata. Gonzalo S. Saldías was partially supported by COPAS Coastal (ANID FB210021) and Fondecyt Grant 1220167. Roberto Aedo-García was partially supported by the Department of Physics at the Universidad del Bío-Bío. Carlos Rey was partially supported by ANID Subvención a la Instalación en la Academia (grant 85220108) and VRIP-UBB (grant RE2360219). We thank two anonymous reviewers for their constructive comments, which significantly improved the original version of this manuscript.

Appendix 6

See Table 9.

Data availability

The complete Ñuble Region dataset used in this study is openly available through the Zenodo repository at https://doi.org/10.5281/zenodo.17234793. The repository includes raw dual-channel voltage traces, expert-interpreted hydraulic conductivity profiles (`HydCon(Z)`), station geolocation files (KML/KMZ), and borehole drilling logs. The data are distributed under a Creative Commons CC-BY 4.0 licence and can be accessed without restriction.

References

Abbas, M., Deparis, J., Isch, A., Mallet, C., Jodry, C., Azaroual, M., Abbar, B., Baltassat, J., 2022. Hydrogeophysical characterization and determination of petrophysical parameters by integrating geophysical and hydrogeological data at the limestone vadose zone of the Beauce aquifer. J. Hydrol. http://dx.doi.org/10.1016/j.jhydrol.2022.128725.

Aguirre, I., Maringue, J., Santibáñez, I., Yáñez, G., 2022. The role of the geophysical exploration in deep aquifers in semi-urban and rural environments in Andean forearc basins, study case in the aquifer of Ñuble river, Central valley of Chile. Andean Geol. 49 (1), 18–54. http://dx.doi.org/10.5027/andgeoV49n1-3370.

Ahmadisharaf, A., Nematirad, R., Sabouri, S., Pachepsky, Y., Ghanbarian, B., 2024. Representative sample size for estimating saturated hydraulic conductivity via machine learning: A proof-of-concept study. Water Resour. Res. 60, http://dx.doi.org/10.1029/2023wr036783.

Albalasmeh, A., et al., 2022. Artificial neural network optimization to predict saturated hydraulic conductivity in arid and semi-arid regions. Catena 217, 106459. http://dx.doi.org/10.1016/j.catena.2022.106459.

Alvarez-Garreton, C., Boisier, J.P., Garreaud, R., Seibert, J., Vis, M., 2021. Progressive water deficits during multiyear droughts in basins with long hydrological memory in Chile. Hydrol. Earth Syst. Sci. 25, 429–446. http://dx.doi.org/10.5194/hess-25-429-2021.

Binley, A., Cassiani, G., Deiana, R., 2010. Hydrogeophysics: opportunities and challenges. Boll. Geofis. Teor. Appl. 51 (4), 267–284, URL: https://bgo.ogs.it/sites/default/files/pdf/bgta51.4_Binley.pdf.

Binley, A., Hubbard, S.S., Huisman, J.A., Revil, A., Robinson, D.A., Singha, K., Slater, L.D., 2015. The emergence of hydrogeophysics for improved understanding of subsurface processes over multiple scales. Water Resour. Res. 51 (6), 3837–3866. http://dx.doi.org/10.1002/2015WR017016.

Boisier, J.P., Alvarez-Garreton, C., Marinao, R., Galleguillos, M., 2025. Increasing water stress in Chile revealed by novel datasets of water availability, land use and water use. Hydrol. Earth Syst. Sci. 29, 5185–5212. http://dx.doi.org/10.5194/hess-29-5185-2025.

Chicco, J., Comina, C., Mandrone, G., Vacha, D., Vagnon, F., 2023. Field surveys in heterogeneous rock masses aimed at hydraulic conductivity assessment. SN Appl. Sci. 5, 1–20. http://dx.doi.org/10.1007/s42452-023-05578-3.

Cosenza, P., Ghorbani, A., Camerlynck, C., Rejiba, F., Guérin, R., Tabbagh, A., 2009. Effective medium theories for modelling the relationships between electromagnetic properties and hydrological variables in geomaterials: a review. Near Surf. Geophys. 7 (5–6), 563–578. http://dx.doi.org/10.3997/1873-0604.2009009.

Costa, A., 2006. Permeability-porosity relationship: A reexamination of the Kozeny-Carman equation based on a fractal pore-space geometry assumption. Geophys. Res. Lett. 33 (2), http://dx.doi.org/10.1029/2005GL025134.

Dumont, M., Singha, K., 2024. Geophysics as a hypothesis-testing tool for critical zone hydrogeology. Wiley Interdiscip. Rev.: Water 11, http://dx.doi.org/10.1002/wat2.1732.

Fan, J., Meiliya, Y., Wu, S., Du, G., Chen, L., 2025. A double-layered seismo-electric method for characterizing groundwater seepage fields in high-level waste disposal. Water http://dx.doi.org/10.3390/w17192848.

Feng, F., Ghorbani, H., Radwan, A.E., 2024. Predicting groundwater level using traditional and deep machine learning algorithms. Front. Environ. Sci. 12, 1291327. http://dx.doi.org/10.3389/fenvs.2024.1291327.

Friedel, S., 2003. Resolution, stability and efficiency of resistivity tomography estimated from a generalized inverse approach. Geophys. J. Int. 153 (2), 305–316. http://dx.doi.org/10.1046/j.1365-246X.2003.01890.x.

Garreaud, R.D., Alvarez-Garreton, C., Barichivich, J., Boisier, J.P., Christie, D.A., Galleguillos, M., LeQuesne, C., McPhee, J., Zambrano-Bigiarini, M., 2017. The 2010–2015 megadrought in central Chile: Impacts on regional hydroclimate and vegetation. Hydrol. Earth Syst. Sci. 21, 6307–6327. http://dx.doi.org/10.5194/hess-21-6307-2017.

Garreaud, R.D., Boisier, J.P., Rondanelli, R., Montecinos, A., Sepúlveda, H.H., Veloso-Aguila, D., 2020. The central Chile mega drought 2010–2018: A climate dynamics perspective. Int. J. Climatol. 40 (1), 421–439. http://dx.doi.org/10.1002/joc.6219.

Grobbe, N., Revil, A., Slob, E., Zhu, Z., 2020. Seismoelectric Exploration: Theory, Experiments, and Applications. Geophysical Monograph Series, American Geophysical Union.

Hu, K., Ren, H., Huang, Q., Zeng, L., Butler, K.E., Jougnot, D., Linde, N., Holliger, K., 2023. Water table and permeability estimation from multi-channel seismoelectric spectral ratios. J. Geophys. Res.: Solid Earth 128 (5), e2022JB025505. http://dx.doi.org/10.1029/2022JB025505.

Huang, Q., Wu, S., Xue, J., 2025. Data science and machine learning in geoelectromagnetics: A review. Surv. Geophys. 1–56. http://dx.doi.org/10.1007/s10712-025-09904-9.

Jardani, A., Revil, A., Bérard, V., Crespy, A., 2007. Tomography of the Darcy velocity from self-potential measurements. Geophys. Res. Lett. 34 (24), L24403. http://dx.doi.org/10.1029/2007GL031907.

Jarzyna, J., Puskarczyk, E., Motyka, J., 2019. Estimating porosity and hydraulic conductivity for hydrogeology on the basis of reservoir and elastic petrophysical parameters. J. Appl. Geophys. http://dx.doi.org/10.1016/J.JAPPGEO.2019.05.012.

Jiang, S., Zhang, R., Liu, J., Xia, X., Li, X., Zheng, M., 2022. Simultaneous estimation of a contaminant source and hydraulic conductivity field by combining an iterative ensemble smoother and sequential Gaussian simulation. Water http://dx.doi.org/10.3390/w14050757.

Koch, K., Kemna, A., Irving, J., Holliger, K., 2011. Impact of changes in grain size and pore space on the hydraulic conductivity and spectral induced polarization response of sand. Hydrol. Earth Syst. Sci. 15, 1785–1794. http://dx.doi.org/10.5194/hess-15-1785-2011.

LeDell, E., Poirier, S., 2020. H2O AutoML: Scalable automatic machine learning. In: Proceedings of the AutoML Workshop at ICML.

Legates, D.R., McCabe Jr., G.J., 1999. Evaluating the use of "goodness-of-fit" measures in hydrologic and hydroclimatic model validation. Water Resour. Res. 35 (1), 233–241. http://dx.doi.org/10.1029/1998WR900018, arXiv:https://agupubs.onlinelibrary.wiley.com/doi/pdf/10.1029/1998WR900018, URL: https://agupubs.onlinelibrary.wiley.com/doi/abs/10.1029/1998WR900018.

Li, X., Slater, L., Binley, A., Wang, Z., 2022. Estimating permeability using deep learning and geophysical data: A comparison of architectures and feature selection. Adv. Water Resour. 159, 104085. http://dx.doi.org/10.1016/j.advwatres.2021.104085.

Lochbuhler, T., Doetsch, J., Brauchler, R., Linde, N., 2013. Structure-coupled joint inversion of geophysical and hydrological data. Geophysics 78, http://dx.doi.org/10.1190/geo2012-0460.1.

Martínez-Ballesta, M., Rodríguez-Hernández, M., Alcaraz-López, C., Mota-Cadenas, C., Muries, B., Carvajal, M., 2011. Hydraulic Conductivity-Issues, Determination and Applications. In Tech.

Martins-Gomes, V., Brito, D., Garambois, S., Dietrich, M., Bordes, C., Barucq, H., 2023. Seismoelectric wave conversions at an interface: a quantitative comparison between laboratory data and full-waveform modelling. Geophys. J. Int. http://dx.doi.org/10.1093/gji/ggad409.

Medici, G., West, L., 2021. Groundwater flow velocities in karst aquifers; importance of spatial observation scale and hydraulic testing for contaminant transport prediction. Environ. Sci. Pollut. Res. 28, 43050–43063. http://dx.doi.org/10.1007/s11356-021-14840-3.

Moriasi, D.N., Arnold, J.G., Van Liew, M.W., Bingner, R.L., Harmel, R.D., Veith, T.L., 2007. Model evaluation guidelines for systematic quantification of accuracy in watershed simulations. Trans. ASABE 50 (3), 885–900. http://dx.doi.org/10.13031/2013.23153.

Moriasi, D.N., Gitau, M.W., Pai, N., Daggupati, P., 2015. Hydrologic and water quality models: Performance measures and evaluation criteria. Trans. ASABE 58 (6), 1763–1785. http://dx.doi.org/10.13031/trans.58.10715.

Nam, S., Gutierrez, M., Diplas, P., Petrie, J., 2021. Laboratory and in situ determination of hydraulic conductivity and their validity in transient seepage analysis. Water 13 (8), 1131. http://dx.doi.org/10.3390/w13081131.

Nguyen, T.-T.-H., Vu, D.-Q., 2024. Predicting hydraulic conductivity using machine learning techniques. Res. Sq. http://dx.doi.org/10.21203/rs.3.rs-4509834/v1, URL: https://doi.org/10.21203/rs.3.rs-4509834/v1.

Oldenborger, G.A., Paradis, D., 2023. Hydraulic conductivity estimation and lithological classification of an esker aquifer system using surface electrical resistivity surveys and a neural network. J. Appl. Geophys. 215, 105106. http://dx.doi.org/10.1016/j.jappgeo.2023.105106.

Osta, M.E., Masoud, M., Alqarawy, A., Badran, O., 2023. Utilizing of aquifer hydraulic parameters to assess the groundwater sustainability in the new reclamation area of Moghra Oasis: Western Desert-Egypt. Appl. Water Sci. 13, http://dx.doi.org/10.1007/s13201-023-02042-w.

Pride, S.R., 1994. Governing equations for the coupled electromagnetics and acoustics of porous media. Phys. Rev. B 50 (21), 15678–15696. http://dx.doi.org/10.1103/PhysRevB.50.15678.

Radwan, A.E., Ghorbani, H., et al., 2022. Predicting shear wave velocity from conventional well logs with deep learning in sandstone and carbonate reservoirs. J. Pet. Explor. Prod. Technol. http://dx.doi.org/10.1007/s13202-022-01531-Z.

ur Rehman, Z., Khalid, U., Ijaz, N., Mujtaba, H., Haider, A., Farooq, K., Ijaz, Z., 2022. Machine learning-based intelligent modeling of hydraulic conductivity of sandy soils considering a wide range of grain sizes. Eng. Geol. 311, 106899. http://dx.doi.org/10.1016/j.enggeo.2022.106899.

Revil, A., Jardani, A., 2013. The Self-Potential Method: Theory and Applications in Environmental Geosciences. Cambridge University Press, http://dx.doi.org/10.1017/CBO9781139094252.

Revil, A., Naudet, V., Nouzaret, J., Pessel, M., 2003. Principles of electrography applied to self-potential electrokinetic sources and hydrogeological applications. Water Resour. Res. 39 (5), 1114. http://dx.doi.org/10.1029/2001WR000916.

Revil, A., Pezard, P.A., 1999. Streaming potential in porous media: 1. Theory of the zeta potential. J. Geophys. Res.: Solid Earth 104 (B9), 20021–20031. http://dx.doi.org/10.1029/1999JB900089.

Revil, A., Schwaeger, H., Cathles, L.M., Manhardt, P.D., 2001. Streaming potential in porous media: 2. Theory and application to geothermal systems. J. Geophys. Res.: Solid Earth 106 (B9), 20041–20052. http://dx.doi.org/10.1029/1999JB900090.

Sánchez-Vila, X., Tartakovsky, D.M., 2007. Ergodicity of pumping tests. Water Resour. Res. 43 (1), http://dx.doi.org/10.1029/2006WR005241.

Servicio Nacional de Geología y Minería, 2003. Mapa geológico de Chile: Versión digital. Escala 1:1.000.000. Publicación Geológica Digital No. 4.

Shepley, M.G., 2024. Vertical hydraulic conductivity and layered heterogeneity: from measurements to models. Hydrogeol. J. 1–26. http://dx.doi.org/10.1007/s10040-024-02773-3.

Sun, D., Luo, N., Vandenhoff, A., McCall, W., Zhao, Z., Wang, C., Rudolph, D.L., Illman, W.A., 2024. Evaluation of hydraulic conductivity estimates from various approaches with groundwater flow models. Groundwater 62 (3), 384–404. http://dx.doi.org/10.1111/gwat.13348.

Thanh, L.D., Jougnot, D., Do, P.V., Ca, N.X., Hien, N.T., 2020. A physically based model for the streaming potential coupling coefficient in partially saturated porous media. Water 12 (6), 1626. http://dx.doi.org/10.3390/w12061588.

Tilahun, T., Korus, J., 2023. 3D hydrostratigraphic and hydraulic conductivity modelling using supervised machine learning. Appl. Comput. Geosci. 19, http://dx.doi.org/10.1016/j.acags.2023.100122.

Trabelsi, F., Bel Hadj Ali, S., Lee, S., 2022. Comparison of novel hybrid and benchmark machine learning algorithms to predict groundwater potentiality: case of a drought-prone region of Medjerda basin, northern Tunisia. Remote. Sens. 15 (1), http://dx.doi.org/10.3390/rs15010152.

Wang, P., Li, F., Lu, K., Huang, W., 2025. Detection of water-rich areas and seepage channels via the transient electromagnetic method, electrical resistivity tomography, and self-potential method. Sci. Rep. 15, http://dx.doi.org/10.1038/s41598-025-00442-3.

Wang, X., Zhang, K., Jiang, S., Song, Y., Jiang, L., He, X., Niu, H., Jiang, W., Li, J., Wu, Y., Gao, Z., Zhang, C., Han, F., Yuan, X., Wang, Y., 2026. Pore characteristics of over-mature to semi-graphitised marine shale: A case study of the Longmaxi Formation, Upper Yangtze Area. Geol. J. 61 (5), 1325–1345. http://dx.doi.org/10.1002/gj.70036.

Wolpert, D.H., 1992. Stacked generalization. Neural Netw. 5 (2), 241–259. http://dx.doi.org/10.1016/S0893-6080(05)80023-1, URL: https://www.sciencedirect.com/science/article/pii/S0893608005800231.

Xie, J., an Cui, Y., Niu, Q., 2021. Coupled inversion of hydraulic and self-potential data from transient outflow experiments to estimate soil petrophysical properties. Vadose Zone J. 20, http://dx.doi.org/10.1002/vzj2.20157.

Zanganeh Kamali, M., Davoodi, S., Ghorbani, H., Wood, D.A., Mohamadian, N., Lajmorak, S., Rukavishnikov, V.S., Taherizade, F., Band, S.S., 2022. Permeability prediction of heterogeneous carbonate gas condensate reservoirs applying group method of data handling. Mar. Pet. Geol. 139, 105597. http://dx.doi.org/10.1016/j.marpetgeo.2022.105597.

Zapata Márquez, N., 2022. Nueva normalidad Hídrica en Chile: Sequía meteorológica en la región de Ñuble. Tiempo Espac. (49), http://dx.doi.org/10.22320/rte.vi49.5826.

Zhang, C., Dong, Y., Wang, Q., Liu, D., She, M., Luo, Q., Dong, X., Huang, Y., Chen, H., Lu, F., 2026. Coupled formation of fracture assemblages in shale and their influence on permeability. Geol. Soc. Am. Bull. 138 (1–2), 177–194. http://dx.doi.org/10.1130/B38277.1.

Zhang, C., Jiang, S., Kong, X., Jiang, Z., Song, Y., Dong, Y., Luo, Q., Song, K., Zhang, K., Lu, F., 2025. What controls oil saturation in fractures? J. Earth Sci. 36 (3), 1315–1319. http://dx.doi.org/10.1007/s12583-025-2030-3.

Zhang, C., Liu, D.-D., Jiang, Z.-X., Song, Y., Luo, Q., Wang, X., 2022. Mechanism for the formation of natural fractures and their effects on shale oil accumulation in Junggar Basin, NW China. Int. J. Coal Geol. 254, 103973. http://dx.doi.org/10.1016/j.coal.2022.103973.

Zhang, C., Zhu, D., Luo, Q., Liu, L., Liu, D., Yan, L., Zhang, Y., 2017. Major factors controlling fracture development in the middle permian lucaogou formation tight oil reservoir, Junggar Basin, NW China. J. Asian Earth Sci. 146, 279–295. http://dx.doi.org/10.1016/j.jseaes.2017.04.032.

Zheng, W., li Hu, X., Tannant, D., Zhou, B., 2021. Quantifying the influence of grain morphology on sand hydraulic conductivity: A detailed pore-scale study. Comput. Geotech. http://dx.doi.org/10.1016/j.compgeo.2021.104147.

Zhu, Z., Chi, S., Zhan, X., Toksöz, M.N., 2008. Theoretical and experimental studies of seismoelectric conversions in boreholes. Commun. Comput. Phys. 3 (1), 109–120. http://dx.doi.org/10.4208/cicp.2008.v3.n1.s8.